Technical Memorandum ERL WPL-171

LIDAR TECHNIQUE FOR MEASURING MULTIPLE FLUORESCENT TRACERS OF ATMOSPHERIC MOTIONS

W. L. Eberhard
Z. Z. Chen

Wave Propagation Laboratory
Boulder, Colorado
August 1989

noaa NATIONAL OCEANIC AND ATMOSPHERIC ADMINISTRATION / Environmental Research Laboratories

NOAA Technical Memorandum ERL WPL-171

LIDAR TECHNIQUE FOR MEASURING MULTIPLE FLUORESCENT TRACERS OF ATMOSPHERIC MOTIONS

W. L. Eberhard
Z. Z. Chen

Wave Propagation Laboratory
Boulder, Colorado
August 1989

UNITED STATES
DEPARTMENT OF COMMERCE

Robert A. Mosbacher
Secretary

NATIONAL OCEANIC AND
ATMOSPHERIC ADMINISTRATION

Environmental Research
Laboratories

Joseph O. Fletcher
Director

NOTICE

Mention of a commercial company or product does not constitute an endorsement by NOAA Environmental Research Laboratories. Use for publicity or advertising purposes of information from this publication concerning proprietary products or the tests of such products is not authorized.

Although the research described in this Technical Memorandum has been funded in part by the U.S. Environmental Protection Agency, it has not been subjected to Agency policy review and therefore does not necessarily reflect the views of the Agency.

For sale by the National Technical Information Service, 5285 Port Royal Road
Springfield, VA 22161

CONTENTS

LIDAR TECHNIQUE FOR MEASURING MULTIPLE FLUORESCENT TRACERS OF ATMOSPHERIC MOTIONS

W.L. Eberhard and Z.Z. Chen

ABSTRACT

An analytical study demonstrates the feasibility of simultaneous lidar measurement and discrimination of multiple fluorescent tracers of air motions. Past work on single tracers is reviewed, and laboratory measurements of some candidates' fluorescence spectra are reported. The characteristics of fluorescent materials, lidar components, and potential interfering signals are summarized. Matrix methods are presented that can solve for the concentrations of several tracers from simultaneous measurements in at least as many spectral receiver channels, even when fluorescence spectra overlap. Two example systems, one with strong crosstalk and another without, are evaluated for accuracy in the presence of shot noise and calibration errors. Schemes for calibration are suggested. Objectives for a field demonstration of the concept are outlined. Potential applications include measuring the effect of release location on atmospheric transport and dispersion and observing the structure of complex flows.

1. INTRODUCTION

Studies of atmospheric transport and diffusion rely heavily on tracers to reveal the air motions. Novel or improved tracer-detector systems can create opportunities for observation of atmospheric dynamics in circumstances that previously have proved difficult or impossible. This study investigates the potential of lidar to detect and discriminate between multiple fluorescent tracers.

A fluorophore absorbs part of the incident light within a specific excitation band of wavelengths. Emission quickly occurs in a different band shifted to longer wavelengths (Lakowicz, 1983). Lidar mapping of a plume or cloud containing a single fluorescent tracer has been accomplished a number of times (Rowland and Konrad, 1979b; Uthe et al., 1985b). Various fluorescent materials have different spectral signatures in emission, making possible the discrimination of their individual concentrations.

Johnson (1983) briefly reviewed tracer techniques, giving the following as key requirements for their effective and efficient use: (1) low background concentrations; (2) faithful tracking of air motions; (3) low, or predictable, transformation and removal processes; (4) easy handling and dispensability; (5) accurate measurement of emission rate; (6) sensitive detection of low atmospheric concentrations; (7) environmental safety; and (9) reasonable cost. One can include in item 6 the requirement for negligible interference from other tracers or substances. No tracer is perfect in all respects, so experimentalists choose those best suited for a particular application.

This study shows that multiple fluorescent particles detected by lidar can fulfill these requirements quite well for some applications. Portions of this report will also appear in

Eberhard and Chen (1989). Although the proposed technique is not without limitations, its high potential arises out of two special characteristics. First, the concentrations of several tracers can be sensed simultaneously. Second, the remote-sensing lidar achieves unparalleled spatial and temporal coverage of tracer distributions by acquiring many profiles in rapid succession. This combination holds promise of revealing flow and turbulence behavior (Sec. 11) in ways not possible before.

1.1 Preceding Development

1.1.1 Previous methods of sample collection and laboratory analysis

The earliest use of fluorescent tracers (FTs) as atmospheric tracers (Leighton et al., 1965) involved in situ sampling. Particles roughly 2 μm in diameter were dispensed from a ground-based high-speed blower at rates between 1 and 250 g min^{-1} or at 22 kg min^{-1} from an aircraft. The particles, developed for use as luminescent paint pigments, contained zinc-inorganic compounds for fluorescence. Airflow filters proved best for total dosage measurements at the surface. For time-resolved measurements, a drum impactor performed well. A Rotorod sampler attached to the cable of a captive balloon was the method of choice for elevated sampling. Human counting of individual fluorescent particles illuminated by ultraviolet light under a microscope was the initial analysis method. Later, automatic photoelectric counting was developed for high-concentration samples. The long emission lifetime of the zinc compounds (Leighton et al., 1965; Voedisch, 1973), typically 10^{-3} s, prohibits their adequate detection by pulsed lidar.

1.1.2 Early lidar demonstration projects of a single tracer

Rowland and Konrad (1979a,b) used a pigment with organic dyes in the first attempt at lidar tracking of a plume of an FT. These pigment particles, which were developed to exhibit bright colors when illuminated by daylight, possess emission lifetimes (Rowland and Konrad, 1979b; Lakowicz, 1983) usually shorter than the pulse length of a lidar. Rowland and Konrad (1979b) measured representative excitation and emission spectra for a number of these commercial pigments, including a determination of the absolute fluorescence efficiencies. During field measurements, a blower dispensed the Fire Orange pigment tracer at typically 1 g s^{-1}. The lidar transmitter for exciting fluorescence was a frequency-doubled Nd:YAG laser with 10–mJ pulse energy at 532–nm wavelength. The receiver consisted of a 15-cm–diameter telescope, blocking and narrowband (approximately 7–nm passband) filters, and a photomultiplier detector.

They reported that the bright daytime background prevented detection of the tracer in low plume concentrations. In the darkness after sunset, they determined a detection threshold of only 0.4 μg m^{-3} at 400–m range for a single pulse of their demonstration equipment. They also considered the sensitivity threshold set by background light and "natural" aerosol fluorescence in a simple analysis. This experimental work (Rowland and Konrad, 1979b) clearly demonstrated the feasibility of a single FT tracked by lidar for observing the behavior of a plume in the atmosphere.

During the same time frame, Schuster and Kyle (1980) analytically examined the potential for lidar detection of an FT. Compared with using elastic (unshifted wavelength) scatter from smoke or some other aerosol particle, they showed the advantage of low background fluorescence for detecting the FT. They recommended that a fluorescent lidar should also obtain information in a second elastic-scatter channel. An example showed that daytime skylight from molecular and aerosol scattering of visible sunlight would severely limit detection of an FT. The signal in the lidar receiver from the steady fluorescence of a tracer illuminated by sunlight would be orders of magnitude smaller. They concluded that CW (continuous-wave) or pulsed lidar detection of a fluorescent tracer at night would have excellent signal-to-background ratio, or in our terminology, signal-to-interference ratio (SIR).

Kyle et al. (1982) also provided experimental confirmation. A sonic nozzle dispensed a 2% slurry of diluted Fire Orange ink pigment into the exhaust of a ventilation stack. The fluorescent particle (FP) release rate amounted to about 10^{-3} g s^{-1}. The lidar's dye laser transmitted 150-mJ pulses at 490-nm wavelength; the receiving telescope had an effective aperture diameter of 63 cm. Kyle et al. encountered problems with filter leakage of the elastic scatter and weak fluorescence generated inside the lidar. They reported a sensitivity at unity signal-to-noise ratio (SNR) of 2.2 $\times$ 10^{-3} μg m^{-3} tracer concentration at 1-km range in a 100-m range gate.

Karl (1988, 1989) demonstrated fluorescent lidar detection of spores and vegetative cells of common, harmless bacteria. A KrF laser transmitted 0.5 J per pulse at 248-nm wavelength. The telescope with 40-cm-diameter primary had special UV high-reflectance coatings. A dichroic beam splitter and two photodetectors permitted simultaneous detection of elastic scatter and fluorescence. The system detected concentrations of 0.3 *Bacillus globiggi* (BG) spores/cm^3 in plumes at 600-m range with SNR of 2 with a single shot, presumably at night. The cultured BG cells, which have stronger fluorescence at shorter wavelength than the spores, are attractive for detection in the 280-340 nm band with the peak near 310 nm. The portion of the emission below 300 nm is in the solar-blind region, where ozone absorption makes background light negligible. This tracer should perform well even in daytime, but attenuation by ozone absorption and strong Rayleigh scatter should be compensated during processing in quantitative applications.

1.1.3 Lidar field applications of a single tracer

The technique was applied in a variety of case studies (Uthe et al., 1985b) during the Cross-Appalachian Tracer Experiment (CAPTEX '83). These case studies were also reported in conference papers (Ching et al., 1984; Uthe et al., 1985a), and some additional details can be found in Uthe et al. (1984). Fire Orange tracer was dispensed from an aircraft and observed by a downward-looking lidar in a separate airplane. Excitation was by a frequency-doubled Nd:YAG laser emitting approximately 10 mJ at 532-nm wavelength and maximum 10-Hz pulse rate. Elastic scatter of the 1064-nm fundamental wavelength was detected simultaneously.

Several examples were cited showing the value of the FT lidar method. In one case, a cloud containing 50 kg of tracer was tracked at night to 327 km distance downwind of

the release point. In a second case study, the aircraft performed repeated traverses above a tracer cloud to reveal its three-dimensional shape as far as 150 km downwind of release. On another occasion, a puff of tracer was released near the source of a power plant plume, and the elastic scatter from the plume and fluorescence from the tracer were compared as far as 29 km downwind. The divergence of two tracer clouds released at different heights was observed on another experiment night. A tracer cloud transported across land/sea interfaces at Lake Ontario was observed to undergo changes in vertical motion and horizontal dispersion. Tracer puffs were released at various locations relative to fair-weather cumulus clouds, and some success was achieved in the afternoon in observing puff motions before strong dilution by turbulent mixing. An airborne platform for the fluorescent lidar is ideal for bringing the instrument close enough to the tracer for satisfactory SNR at a low detection threshold.

This body of work on single fluorescent tracers guides the development of the multiple fluorescent tracer concept and gives credence to potential applications.

1.2 Multiple Tracers

This study demonstrates analytically the feasibility of lidar tracking of multiple fluorescent tracers. The development is based on laboratory measurements and well-established lidar principles. The optical and physical characteristics of some readily available tracers and the characteristics of lasers and other lidar hardware are considered. Sources of interfering signals and equations for SIR and SNR are given, including the effects of shot noise. The matrix equations for solving the lidar signals for the concentrations of multiple tracers are presented. The performance of a candidate two-tracer system is simulated, and a sensitivity analysis for the presence of crosstalk between tracers in the presence of shot noise is performed. Potential applications are listed and calibration procedures discussed.

A field demonstration, supported by additional laboratory and analytical studies, is the next logical step in development of the multiple-FT lidar technique.

2. CONCEPT FOR MULTIPLE FLUORESCENT TRACER LIDAR

The multiple-FT lidar technique requires FT types with different emission spectra. The important spectral characteristics of a multiple-FT lidar are illustrated in Fig. 1. In this example, a lidar simultaneously transmits a pulse of energy at two well-separated wavelengths. The shorter laser wavelength (l = 1) is near the peak of the excitation band of the p = 1 type of fluorescent particle (lower dashed line). It fluoresces in a broad band (middle dashed line) typically ~100 nm wide. One optical channel of the receiver has a filter and detector passband (d = 1, top dashed line) that unambiguously measures the amount of emission in the shaded region for p = 1.

The longer laser wavelength (l = 2) excites two tracers (p = 2 and 3), which have partially overlapping emission spectra. Receiver channel d = 4 can unambiguously measure the fluorescence from p = 3, although this signal is weak because it comes from the

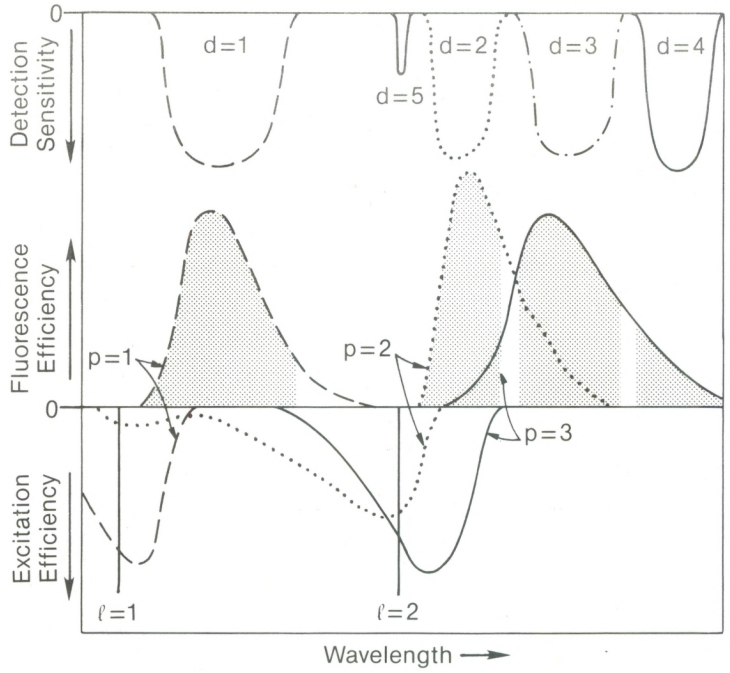

Figure 1. Spectral relationships in a lidar system observing three tracers. At the bottom, two laser wavelengths (l = 1,2) intersect the excitation spectra of the three types of fluorescent particles (p = 1–3). The receiver channels d = 1–4 (top) detect the fluorescent emission spectra (middle) in the shaded wavelength bands. The fifth detector measures the on-line scatter from wavelength l = 2.

tail of the emission spectrum. Channel d = 3 responds mainly to emission from p = 3, but also receives a substantial contribution from p = 2. Similarly, channel 2 is centered near the peak of p = 2, but also receives signal from tracer p = 3. Data from channels 2–4 must be considered jointly to determine the concentration of tracer 2.

The hardware could be simplified by eliminating one receiver channel (d = 2, 3, or 4) and still using the measurements from the remaining two to solve simultaneously for the concentrations of tracers 2 and 3. Note also that the shorter wavelength excites tracer 2 (dotted line) by a small additional amount, but this does not complicate the discrimination between tracers 2 and 3.

Another receiver channel (d = 5) could detect the on-line scatter at one of the laser wavelengths. This would be valuable for observing the distribution of ambient aerosol particles and tracking nonfluorescent tracers.

A block diagram of a lidar corresponding to the scenario in Fig. 1 is shown in Fig. 2. The system is similar to those detecting elastic scatter at more than one wavelength (e.g., Eberhard and McNice, 1986), except that the multiple-FT lidar must handle the fluorescent shifts and possess more optical channels in the receiver. Lidars that profile water vapor using the Raman effect (e.g., Melfi and Whiteman, 1985; Renaut and Capitini, 1988) are even closer in form to the envisioned multiple-FT lidar.

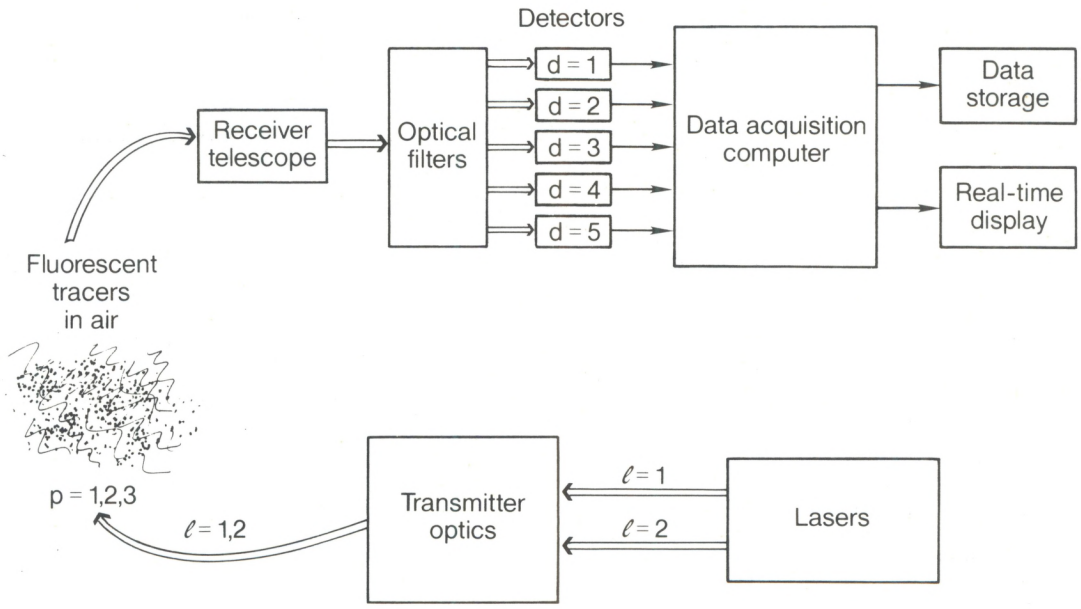

Figure 2. Block diagram of lidar system corresponding to Fig. 1.

The two transmitted wavelengths in this example might be generated by two separate lasers. Alternatively, the transmitter might include only one laser, part of whose energy is converted by frequency multiplication or wavelength shifting.

The optical discrimination by filtering in the receiver is a key part of the multiple-FT lidar that will be rather complex. Two filtering methods have good potential. One method uses beam splitters followed by an interference filter before each detector (Rowland and Konrad, 1979b; Uthe et al., 1985b; Melfi and Whiteman, 1985). The other method uses a grating spectrometer. Each detector should be that most suitable for the particular wavelength band.

The data acquisition computer must be able to handle a high data rate. A real-time graphical display is important for two reasons. It is crucial for quality control, because it can immediately warn of most problems that may occur in the lidar system. The display is also extremely valuable for experimental guidance, because it can show, at least in a crude way, the concentration distributions of the tracers. A data storage capability completes the lidar system.

The characteristics of the various components in the lidar system are discussed in more detail in Section 4.

3. FLUORESCENT TRACERS

3.1 Physics of Fluorescence

Lakowicz (1983) described several aspects of fluorescence pertinent to lidar applications. A molecule absorbs a photon and is excited from its ground electronic state S_0 to a

higher state S_1. The transition can be to any of many vibrational levels in S_1, so the excitation band is broad (examples in Sec. 3.4). When in a fluid or solid, the molecule rapidly relaxes to a low (usually ground) vibrational level of S_1 during collisions with surrounding molecules. The fluorescent emission occurs as the molecule emits a photon to decay to S_0, again to any of many excited vibrational levels. Vibrational relaxation to the ground level of S_0 completes the transitions. The emitted photon has less energy and hence longer wavelength than the exciting photon because energy is lost in the vibrational relaxations.

Many fluorophores have a single-peaked emission spectrum skewed in shape with a tail toward longer wavelengths. However, there are many exceptions, such as spectra with multiple peaks. The vibrational levels in S_0 frequently are similar to those in S_1, so the emission spectrum in many cases is a mirror image (roughly) of the excitation spectrum.

The typical lifetimes (Lakowicz, 1983) associated with photon absorption, vibrational relaxation, and fluorescent emission are 10^{-15} s, 10^{-12} s, and 10 ns, respectively. Lasers used in lidars have pulse lengths of usually 10 ns or longer, so the fluorescence process should have little effect on the range-resolving capability of lidar. (A related process is phosphorescence, in which the emission lifetime is much longer because the electronic transition is from the triplet rather than the singlet state. Phosphors do not permit range-resolved measurements.) Rowland and Konrad (1979b) could detect no delayed emission from their tracer candidates when illuminated with 12–ns pulses at 532–nm wavelength and observed by a detector with 3–ns risetime. It is important to check the fluorescent lifetime of each tracer candidate.

Fluorescence is usually partially polarized when excited by linearly polarized light (Lakowicz, 1983), which lidars usually transmit. Fluorophores preferentially absorb photons whose electric vectors are aligned parallel to the molecule's absorption dipoles. This leads to partially polarized emission, even when the molecules are randomly oriented. The degree of emission polarization also depends on the angle between the emission dipole and absorption dipoles, which is usually a function of excitation wavelength. Since emission is only partially polarized, an attempt to use different transmitted polarizations to help discriminate between tracers is not very attractive. Although earlier publications on lidar detection of fluorescent tracers did not address polarization, this is a property that should be considered during design and calibration.

The fluorescence also is affected by the fluorophore's immediate environment. Collision of the excited molecule with O_2 or certain other molecules quenches the emission, so most fluorophores cannot be used in their gas phase in the atmosphere. Fluorescent molecules also easily exchange energy with each other; this self-quenching generally eliminates particles of a pure fluorophore as an effective tracer. The dipole moment of a fluorophore interacts with surrounding molecules, so the excitation and emission spectra depend to some extent on the liquid or solid medium carrying the molecule.

3.2 Tracer Physical Characteristics

A large number of fluorophores have been identified (e.g., Berlman, 1965; Maeda, 1984), but not all are suitable for use as a tracer. Certain physical and spectral properties are required.

3.2.1 Pigment particles

Rowland and Konrad (1979b) demonstrated that fluorescent pigment particles serve well as lidar-detected tracers of air motions. Some manufacturers of this type of pigment are listed in the Appendix. Kyle et al. (1982) and Uthe et al. (1985b) also used the Fire Orange pigment, manufactured by Day-Glo Color Corporation. Cost at this writing for off-the-shelf products is typically $12 (US) per kilogram. Past experience and the availability of spectral information make these fluorescent pigments prime candidates for a multiple fluorescent tracer system. However, it is possible that even better tracers of a different type might be developed.

Voedisch (1973) and sales literature describe the pigment particles. One method of manufacture is mixing fluorescent dye(s) with a resin material, permitting the mixture to solidify, and grinding to small particles. An alternative process dyes the fine resin particles. Although details of the mixture are proprietary, Voedisch (1973) listed some of the xanthene and aminonaphthalimide dyes as common fluorescent ingredients. The mixture dilutes the fluorescent particles and achieves high fluorescent efficiency by minimizing quenching. Some of the products contain more than one fluorophore to achieve the desired visual effect. This mixture can broaden the emission spectrum and reduce the effectiveness of the material as one of the multiple tracers for lidar.

Average particle diameter (by weight) varies, but ranges between 2 and 10 μm. Kyle et al. (1982) found a mean diameter (by number) of only 0.3 μm and an ellipsoidal shape in their sample of Fire Orange particles. Uthe et al. (1985b) reported an average diameter of 2 μm. Specific gravity is about 1.4. Particles can be obtained that are small enough to follow air motions faithfully and with negligible settling if clumping can be avoided when the particles are dispensed.

The particles are environmentally safe. However, as in any dusty area, persons handling large amounts should wear a protective mask. The resin particles are inert and water insoluble. They are easily washed away, even though the dyes used to color the particles can stain badly in pure form.

The particles are durable, but temperatures above about 120°C and certain solvents must be avoided. Although the fluorescent efficiency fades upon extended exposure to ultraviolet radiation (days to months in sunlight), the tracers are stable for time scales appropriate to a tracer experiment.

3.2.2 Harmless spores and bacteria

The bacterial spores and cells used by Karl (1988, 1989) also have potential. Both are reported to be harmless, even if ingested or inhaled. The spores are a common item in

garden supply stores but would be very expensive if large amounts were needed. Laboratory measurements revealed a total fluorescence cross section almost equal to the cell's geometric area. The spherical spores are 0.8 μm in diameter, whereas the rod-shaped cells are 6 by 1 μm. The cells, which can be cultured overnight in a nutrient broth from a small amount of spores, have promise as a very economical tracer. Fluorescent lifetime was not reported, but seems adequately short in the data. The optical stability of the cells after dispersal into the air must be investigated.

These tracers seem adequate for testing and implementing the multiple fluorescent tracer concept, but other tracers that may have superior performance or lower cost should still be sought.

3.3 Dispensing Tracers

Two methods have been used for dispensing fluorescent tracers into the air. Leighton et al. (1965), Rowland and Konrad (1979b), and Uthe et al. (1985b) used a high-speed jet of air from a blower or a crop duster to disperse a dry powder. Kyle et al. (1982) and Karl (1989) sprayed a fine mist of the fluorescent particles in solution. The liquid carrier evaporated in the atmosphere.

Ideally, the fluorescent particles will be dispersed into the air at a controlled, high rate (perhaps as high as 25 g s^{-1}) with little clumping. This is a challenging task with such small particles. A blower can dispense large quantities of tracer, but prevention of clumping becomes more difficult as the rate increases. An anti-dusting agent normally applied to the Day-Glo pigments (S. Streitel; Day-Glo Color Corp., Cleveland, Ohio; personal communication; 1988) should be excluded from FPs used as tracers. The accurate spray method can avoid clumping, but release rate is quite limited. Clumping lowers the sensitivity of the method, complicates calibrations, and can reduce the ability of the tracer to follow air motions. Clumping may also cause more particles to deposit near a surface release, which can be a nuisance for brightly colored tracers. Understanding and improving the dispensing process should be one objective of future research.

3.4 Some Fluorescent Tracer Spectra

3.4.1 Past measurements

Rowland and Konrad (1979b) reported some excitation and emission spectra for 10 fluorescent pigment colors manufactured by Day-Glo Color Corporation. Different particle sizes or resin types were examined for some of the colors for a total of 15 samples. The particles were suspended in dilute concentration in water with the help of a non-fluorescing wetting agent. The spectral fluorescent efficiency was measured near the backscatter (180°) direction in the instrument described by Benson and Kues (1977). Presumably, the bandpasses for excitation and emission were 10 and 5 nm, respectively, and spectra were measured with reference to sodium fluorescein in distilled water. Graphs were limited to single curves: the emission spectrum at the wavelength of peak

excitation; and the excitation spectrum at the wavelength of peak emission. Absolute fluorescent cross sections were also obtained using laser excitation in a separate apparatus.

3.4.2 New measurements

In this project we examined the full excitation-emission matrix of five of the same products plus Invisible Blue (M. C. Goldberg, U.S. Geological Survey, Denver, Colorado, personal communication, 1989) with a spectrofluorometer described by Weiner and Goldberg (1982). The objectives were to obtain more information for our investigation of multiple fluorescent tracers, especially to extend the wavelength range to include 250 through 800 nm. Goldberg's device automatically scanned the entire two-dimensional matrix of excitation and emission wavelengths in steps of 3 nm, with bandpass of 3 and 4 nm for excitation and emission, respectively. The fluorescent reference was Rhodamine B. The spectrofluorometer could measure emission only at an angle 90° from the direction of excitation, instead of the 180° congruent with a lidar's geometry. We expected that the different emission directions would not alter the shape of the spectra much, but the fluorescent cross sections would be affected. Dilute concentrations of particles were suspended in a 70% solution of glycerol in water. The apparatus was calibrated to obtain the absolute fluorescence efficiency. The data are plotted at 9–nm intervals in Figs. 3–8; note that the vertical scale in the last three figures differs from that in the first three.

Of course, no data were produced in the anti-Stokes region where the emission wavelength λ (F) is smaller than that for excitation, λ (X). In order to avoid contamination by the strong elastic scatter, data were acquired only for λ (F) $\geq \lambda$ (X) + 6 nm. Data at λ (F) = 2λ (X) were also contaminated by second-order reflection of the elastic scatter from the monochromator's grating. Although the instrument was designed for measurements out to 800–nm wavelength, artifacts were evident in some of Goldberg's data when the fluorescence at longer emission wavelengths was weak. Regions in Figs. 3–8 are marked where the data values were set to zero because of contamination or lack of measurement.

As is common in fluorescent spectra, the shape of each emission spectrum is roughly independent of excitation wavelength, although the efficiency does vary with excitation wavelength. A noteworthy exception occurs when the emission wavelength is very close to the excitation wavelength.

Figures 3–8 are ordered by increasing wavelength of the strong emission. These differences in emission spectra form the basis for the multiple fluorescent tracer concept.

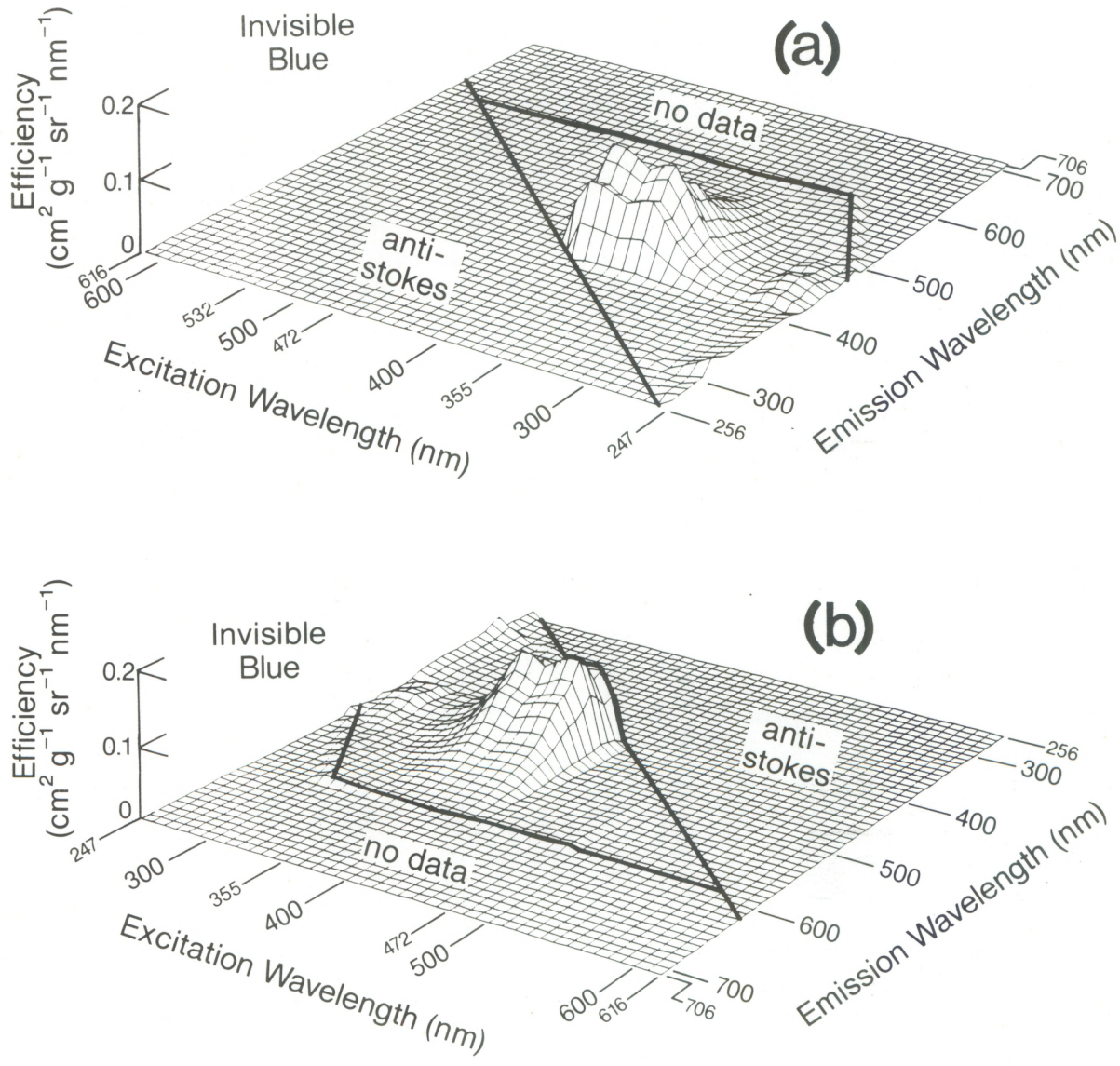

Figure 3. Excitation-emission matrix for Horizon Blue pigment particles. Emission in 90° direction from excitation. (a) View from short-wavelength side; (b) view from long-wavelength side.

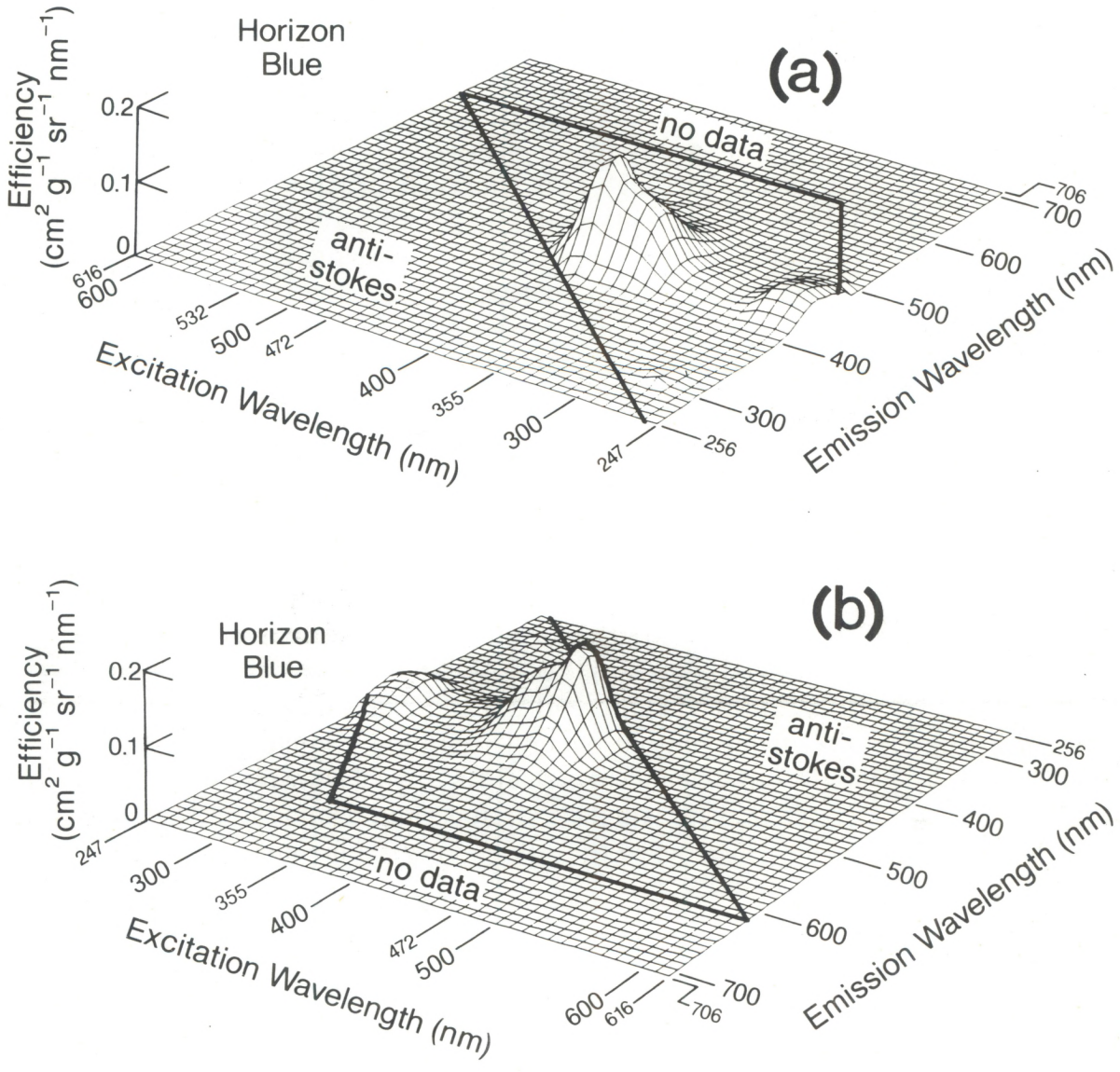

Figure 4. Excitation-emission matrix for Invisible Blue pigment particles. (a) View from short-wavelength side; (b) view from long-wavelength side.

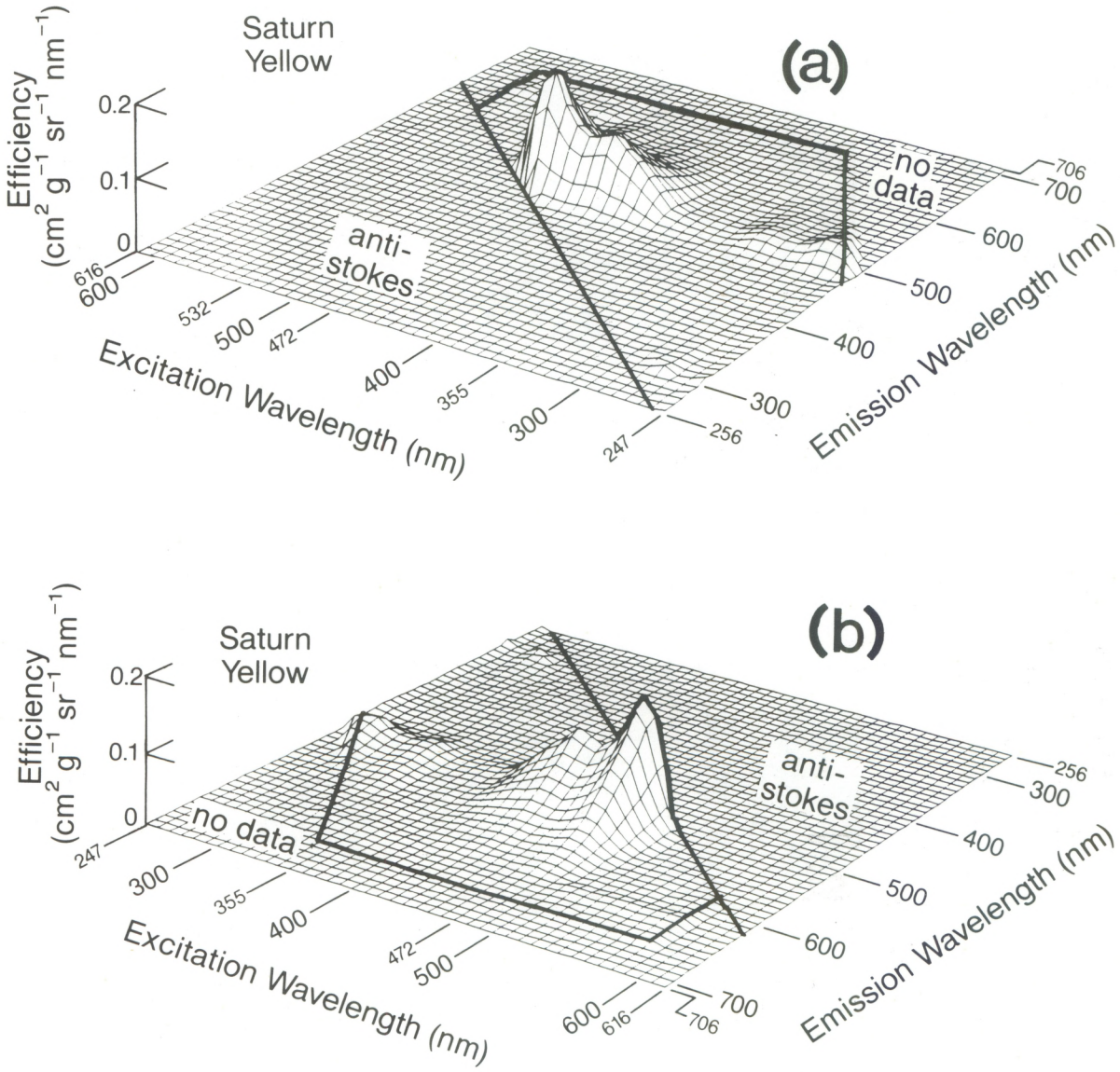

Figure 5. Excitation-emission matrix for Saturn Yellow pigment particles. (a) View from short-wavelength side; (b) view from long-wavelength side.

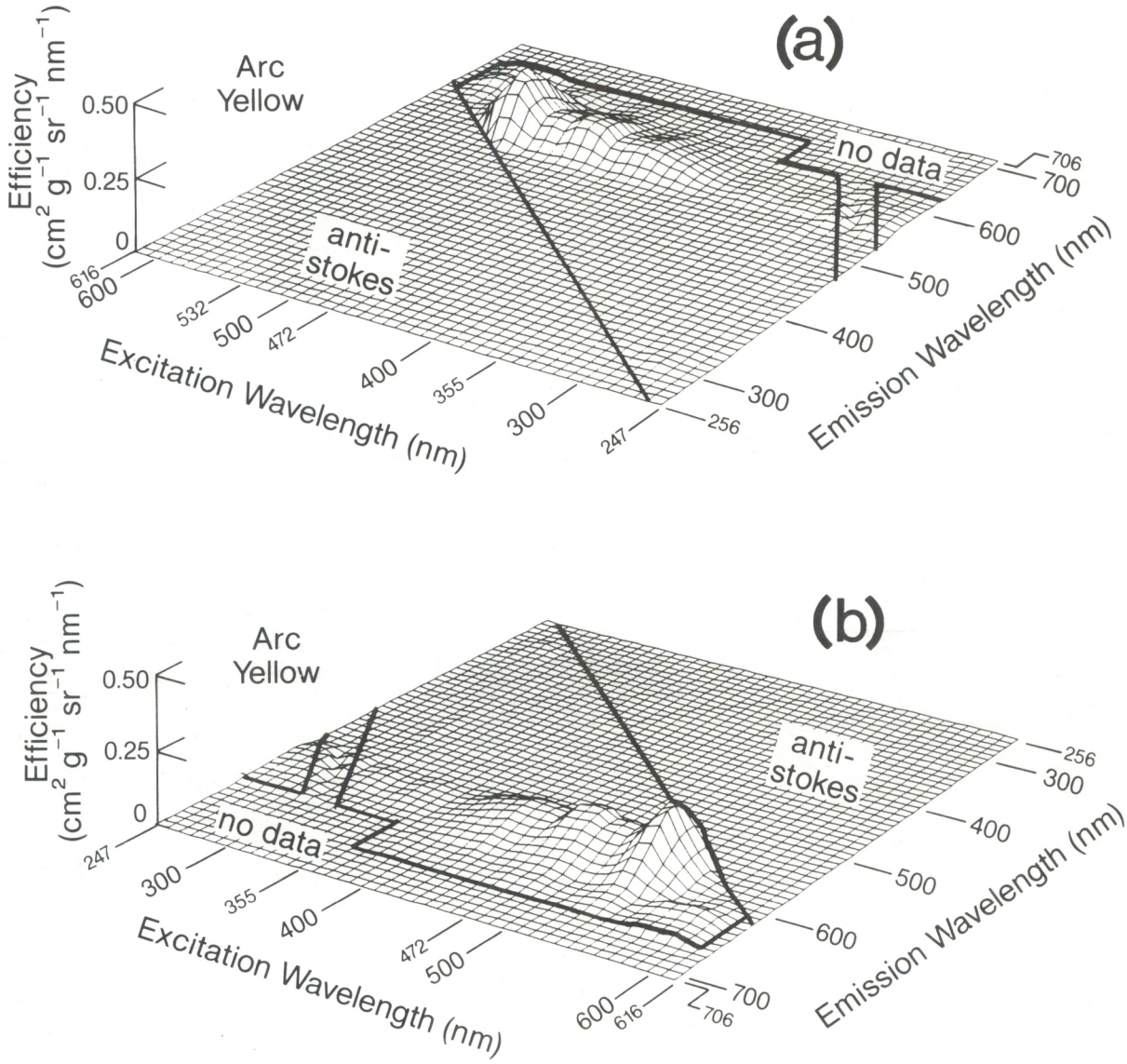

Figure 6. Excitation-emission matrix for Arc Yellow pigment particles. (a) View from short-wavelength side; (b) view from long-wavelength side.

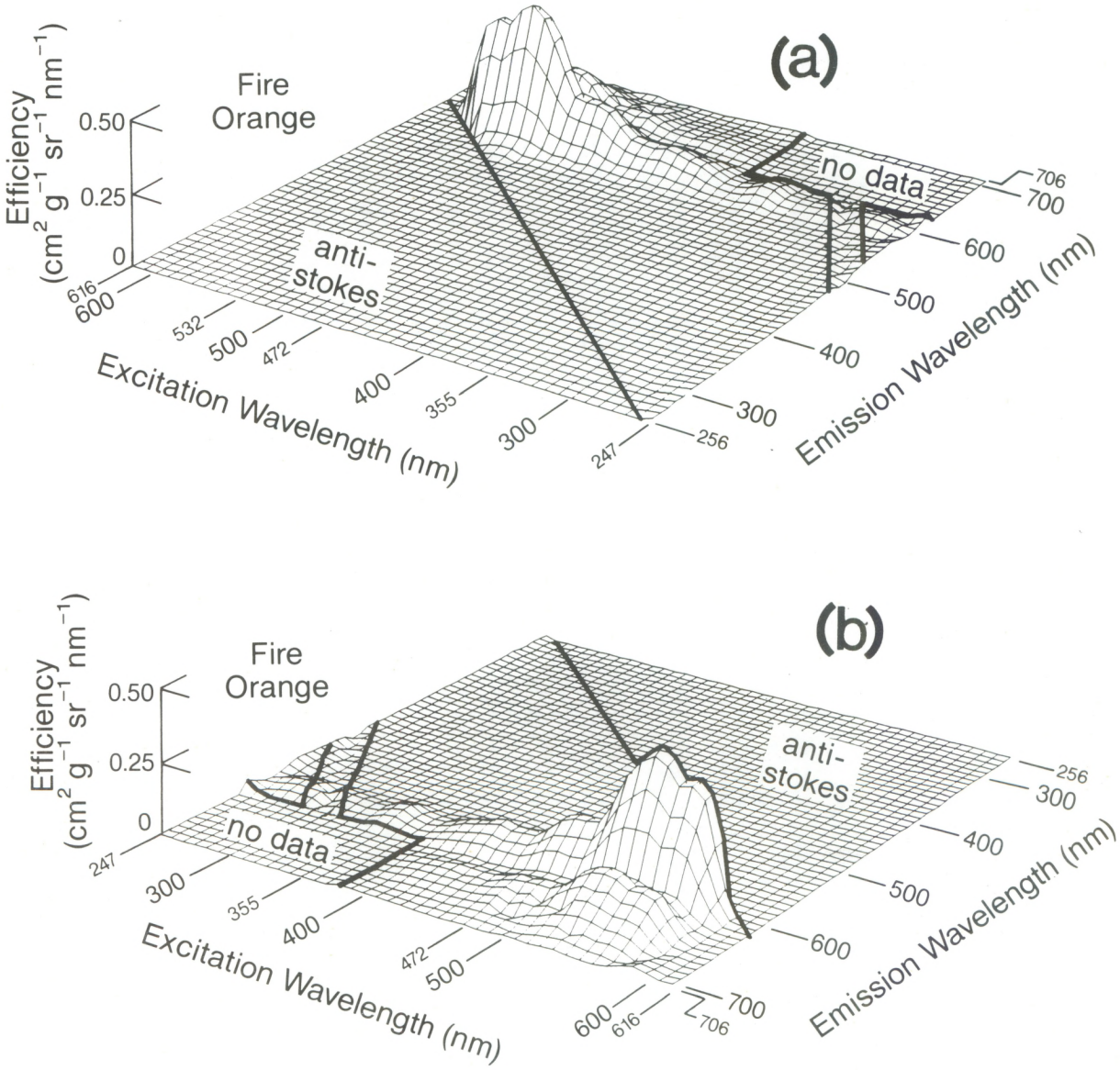

Figure 7. Excitation-emission matrix for Fire Orange pigment particles. (a) View from short-wavelength side; (b) view from long-wavelength side.

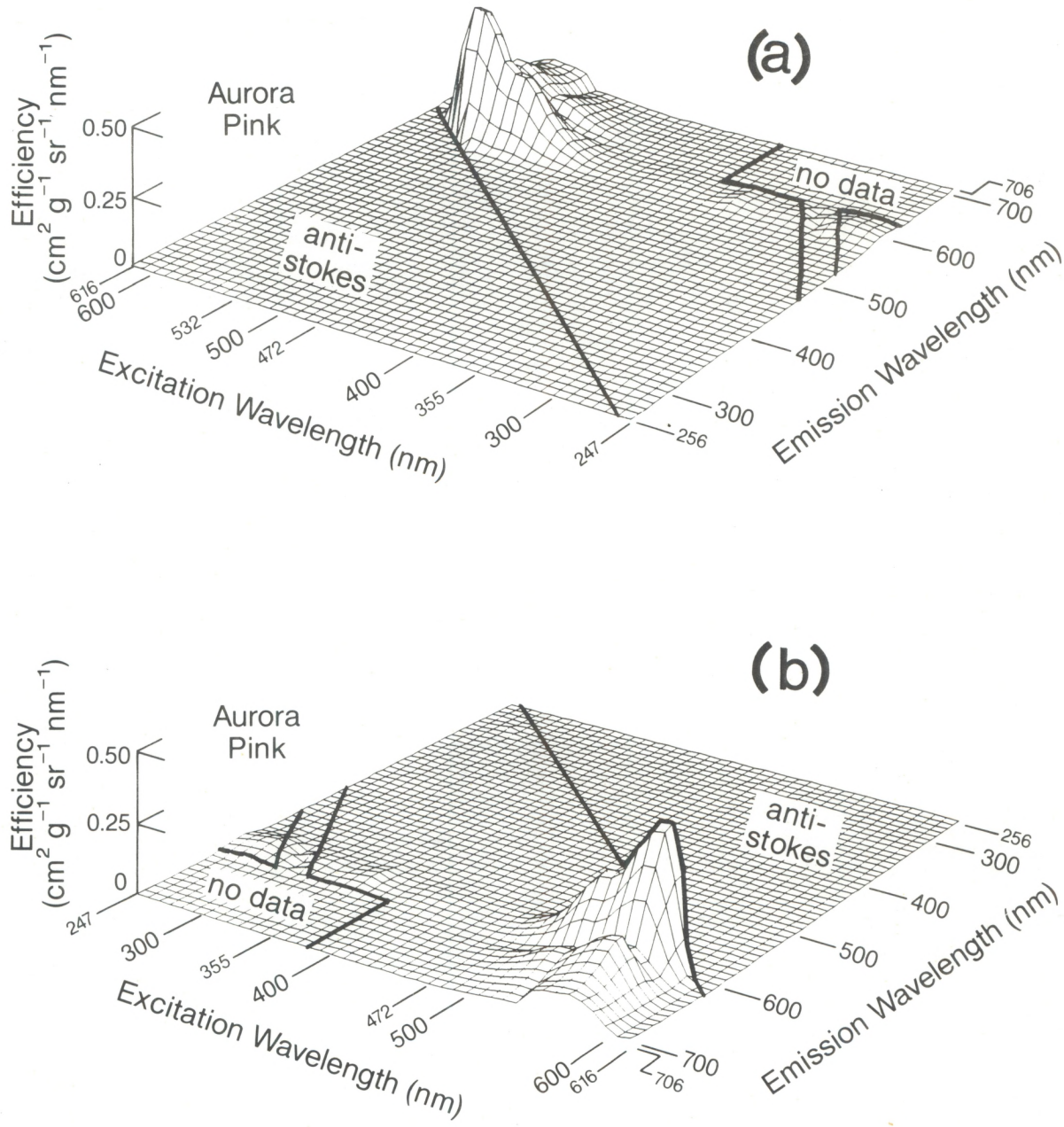

Figure 8. Excitation-emission matrix for Aurora Pink pigment particles. (a) View from short-wavelength side; (b) view from long-wavelength side.

3.4.3 Comparisons

Figures 9–13 compare spectral shapes from our results with those reported in Rowland and Konrad (1979b). Each spectrum was normalized to its peak value. The two methods gave similar results for the gross features of the spectra, but some of the details deviated considerably. The Rowland and Konrad data are heavily smoothed; their curves

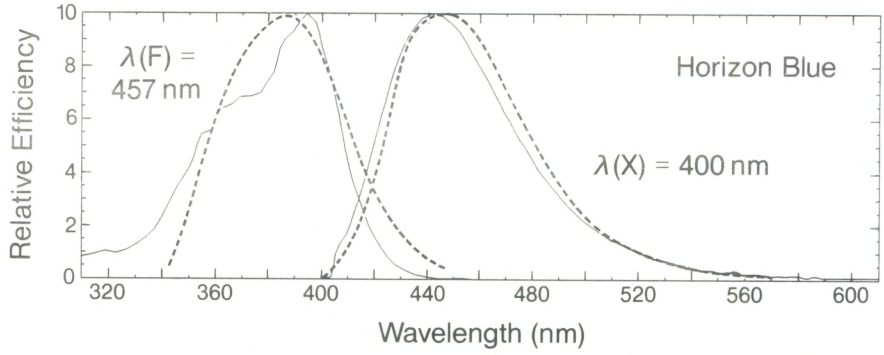

Figure 9. Horizon Blue excitation spectrum for 457–nm emission wavelength and emission spectrum excited by 400 nm wavelength. Solid line: 90° direction (this study); dashed line: near the 180° direction (Rowland and Konrad, 1979b). Each spectrum is normalized to its peak.

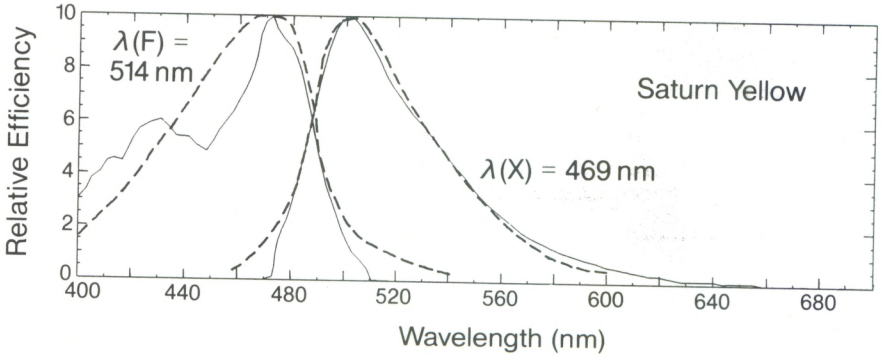

Figure 10. Saturn Yellow excitation spectrum for 514 nm emission wavelength and emission spectrum excited by 469 nm wavelength. (See Fig. 8 legend.)

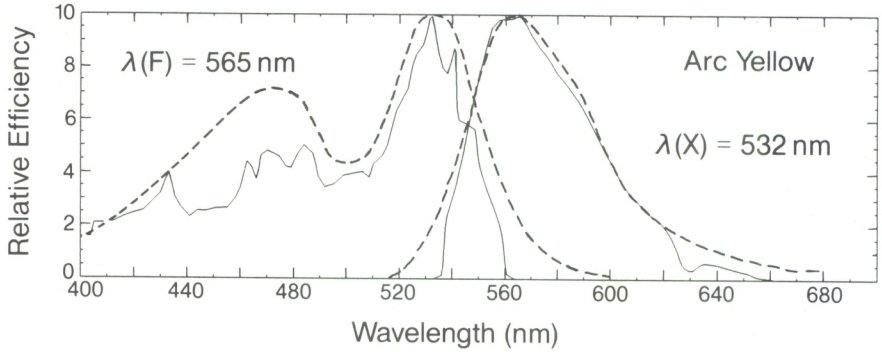

Figure 11. Arc Yellow excitation spectrum for 565 nm emission wavelength and emission spectrum excited by 532 nm wavelength. (See Fig. 8 legend.)

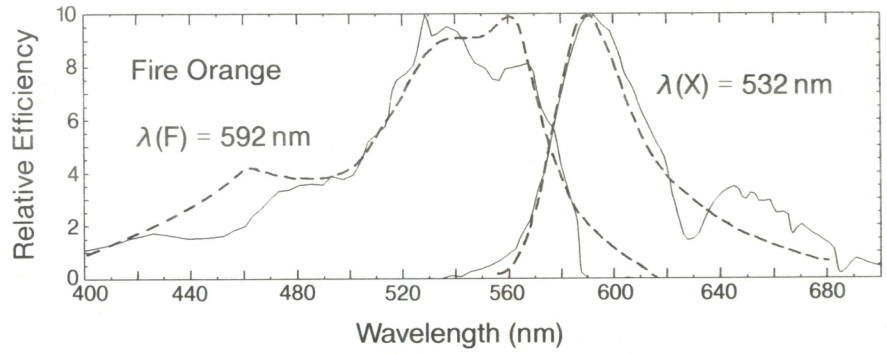

Figure 12. Fire Orange excitation spectrum for 592 nm emission wavelength and emission spectrum excited by 532 nm wavelength. (See Fig. 8 legend.)

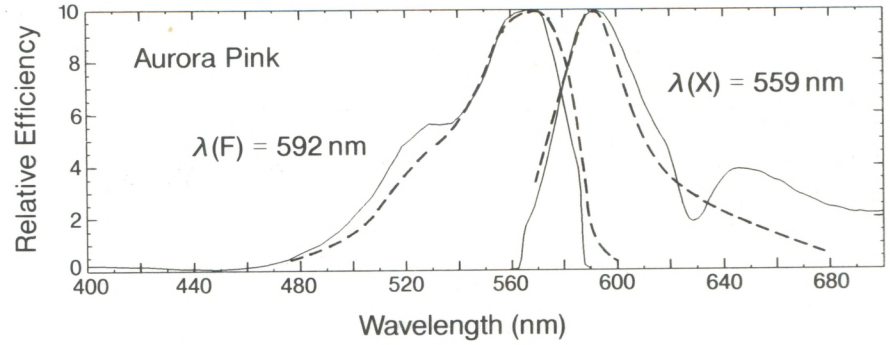

Figure 13. Aurora Pink excitation spectrum for 592 nm emission wavelength and emission spectrum excited by 559 nm wavelength. (See Fig. 8 legend.)

even extend to the anti-Stokes region in some cases. On the other hand, instrument noise appears in some of our data. The dip in our emission spectra at 630 nm and the local maximum at about 642 nm is probably a result of a spectral calibration error. We also note a calibration difference between the two methods at about 450 nm in the excitation spectra.

The peak fluorescent efficiency, (i.e., the cross section for broadband fluorescent emission at the peak in the excitation spectrum), appears in Table 1. Rowland and Konrad (1979b) measured cross sections at either 488 or 515 nm and used the excitation spectrum to calculate the cross section at the excitation peak. Goldberg calibrated his spectrofluorometer at 590 nm, and we used the spectral data to calculate the peak cross section.

Table 1 shows that the wavelength at peak excitation was nearly the same in the two emission directions, except for Fire Orange. Figure 5 demonstrates that the two measurements of Fire Orange actually had similar excitation spectra, but a small difference in the bimodal excitation spectrum (measured at 592-nm-wavelength fluorescence) caused a 28-nm difference in peak wavelength.

Table 1. Peak fluorescent cross sections of some pigment particles at peak excitation wavelength

Pigment*	Near 180° direction (Rowland & Konrad, 1979b)		90°direction (this study)		Cross section ratio (180°/90°)
	λ (X) (nm)	Cross section ($cm^2g^{-1}sr^{-1}$)	λ (X) (nm)	Cross section ($cm^2g^{-1}sr^{-1}$)	
Horizon Blue A-19	390	77	394	10.2	7.5
Invisible Blue A-594-5	358	--	--	9.8	--
Saturn Yellow A-17 @	470	214	472	10.0	21.4
Arc Yellow A-16 @	532	135	532	12.9	10.5
Fire Orange A-14 @	560	194	532	32.2	6.0
Aurora Pink A-11	570	240	565	32.0	7.5

* Day-Glo Color Corporation.
@ Fluorescence in 90° direction for more color-fast samples designated, for example, A-17N.

The peak fluorescent cross sections were considerably smaller for emission at the 90° (or side) direction than near the 180° (back) direction. The ratio was fairly consistent for four of the tracers, varying between 6 and 10.5, but for Saturn Yellow the ratio was considerably larger at 21.4. Scattering calculations by Kerker and Druger (1979) indicated that fluorescent emission from particles depends on polarization, scattering angle, particle size, and index of refraction. Their results indicate that the wavelength-shifted scatter with polarization vertical to the scattering plane (defined by the incident and emitted directions) may be a factor of 2 less at 90° direction than in the back direction at 180°. They show that the deficiency for horizontally polarized emission could even be several times greater. Since Goldberg's spectrofluorometer used unpolarized excitation and detection, a substantial reduction in cross section from 180° to 90° is reasonable.

Other factors certainly caused some of the difference. The dates of manufacture of the samples were separated by several years. The composition of three of the tracers measured at 90° had been changed to make pigments more lightfast. We cannot rule out

the possiblity that the manufacturer changed the recipes in other ways. The glycerol-water solution has slightly higher index of refraction than water alone. And, finally, quantitative accuracy in spectral fluorescence measurements is difficult, and calibration errors may exist.

Although these laboratory measurements are valuable for design purposes, they are inadequate for a careful quantitative calibration of a fluorescent tracer lidar. No laboratory arrangement has yet duplicated the lidar configuration by measuring the fluorescent spectra in the back direction from particles suspended in air.

3.5 Suggestions for Future Research

Several aspects should be addressed in future research to optimize the use of fluorescent tracers.

Dispensing large amounts of such small particles with a minimum of clumping can be difficult. Large clumps will fall out rather than follow air motions faithfully. Clumps, large or small, will diminish the fluorescent cross sections and make the tracer less efficient. Clumping will also introduce uncertainty into the calibration during attempts to measure tracer concentrations accurately. Evaluation and perhaps improvement of aerosol dispensers is needed to ensure adequate dispersal of the tracer.

Bacterial spores and cells should be examined more completely for consistency, optical stability, and practicality. Other spores with different emission spectra might be identified for the multiple tracer concept.

Although fluorescent pigments meet the requirements as single or multiple fluorescent tracers, some improvements may be possible. Pigments with higher fluorescent efficiency (such as the newer AX series from Day-Glo Color Corporation) may be more cost effective and allow better sensitivity. Many of the pigments contain blends of more than one fluorophore. A pigment modified to contain only one desired fluorophore may narrow the emission spectrum and make discrimination between different tracers easier. Perhaps a higher concentration of fluorophore in the resin particles would be better for use with the lidar. An efficient fluorophore with emission in the near infrared could increase the number of tracers that could be used at one time. However, such modifications to improve the normal commercial products may substantially increase manufacturing costs.

Accurate calibration of the fluorescence for the lidar is a challenge. It would be helpful if laboratory methods could be developed that fully mimic lidar measurement of fluorescence at 180° from the particles suspended in air. In any event, field calibrations, discussed in Sec. 9, should be part of any measurement program seeking quantitative accuracy in tracer concentrations.

4. LIDAR COMPONENTS

4.1 Lasers

Commercially available lasers that might be considered for the transmitters in a multiple fluorescent tracer lidar are listed in Table 2, and wavelengths are displayed graphically in Fig. 14. Lidars with transmitters at shorter wavelengths will not perform well because of strong atmospheric absorption. Although adequate fluorescent particles with excitation wavelengths greater than 600 nm have not been identified yet, some fluorophores do exist out to about 1000 nm excitation wavelength (Maeda, 1984). The parameters in Table 2 are intended only as a rough guide to lasers with reasonable cost, size, durability, and power requirements. Considerably higher pulse energy or repetition rate is already available from most of these laser types, but expense, power, cooling, and maintenance requirements can also be much greater. Technological progress can be expected to bring better performance and even lasers at additional wavelengths.

Table 2. Typical characteristics of laser candidates for reasonable fluorescent tracer lidar systems

Laser type	Wavelength (nm)	Pulse energy (mJ)	Pulse rate (Hz)	Aver. power (W)	Pulse resolution (m)	Comments
KrF	248	300	100	30	3	
Nd:YAG (×4)	266	40	20	0.8	3	
XeCl	308	200	100	20	1.5	
Ruby (×2)	347	300	1	0.3	5	
XeFl	351	300	50	15	5	
Nd:YAG (×3)	355	110	20	2.2	3	
Alexandrite (×2)	377	50	4	0.2	7.5	
Copper vapor	511	2	10000	20	7.5	
Nd:YAG (×2)	532	250	20	5	3	
Copper vapor	578	2	10000	20	7.5	
Gold vapor	628	1	5000	5	5	
Ruby	694	2000	1	2	5	
Alexandrite	755	600	4	2.4	20	
Alexandrite	730–780	150	10	1.5	15	Tunable
Ti:sapphire	680–1050	0.4	250	0.1	4	Tunable
Diode stack	850	1.5	5000	7.5	7.5	Big divergence
Diode stack	880	5	1000	5	15	Big divergence
Nd:YAG	1064	700	20	14	3	
Dye (flash-pump)	300–960	150	25	3.75	45	Tunable
Dye (laser-pump)	300–960	50	20	1	2	Tunable

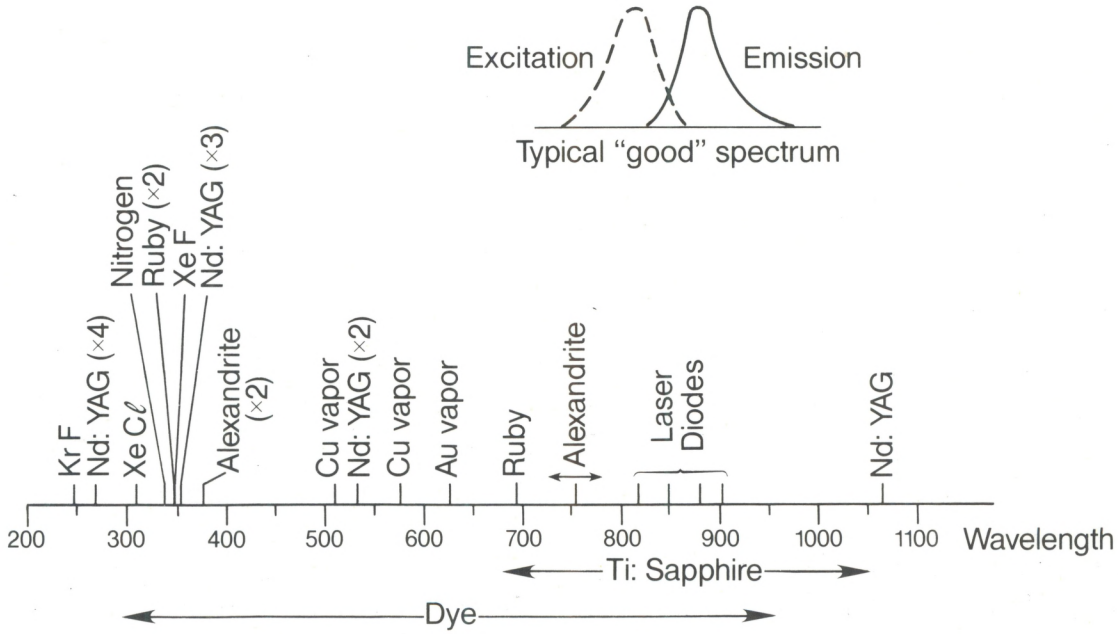

Figure 14. Wavelengths of candidate lasers for a multiple-FT lidar. Widths of typical fluorescent excitation and emission spectra are also shown for comparison.

The lasers with low pulse energy are not very desirable for the fluorescent particle lidar. Sensitivity would be poor, because the SNR of low energy pulses against detector noise would be poor. The high pulse rate could compensate somewhat by averaging many pulses, but this would require an extremely fast data acquisition system. The nitrogen, copper, gold, diode stack, and current Ti:sapphire lasers are therefore not well suited for the fluorescent particle lidar.

The Nd:YAG laser, or any of its harmonics, is an excellent choice because it is efficient, durable, and widely available. This type of laser can produce pulse energies and pulse rates appropriate for the fluorescent lidar. Frequency multipliers can convert part (typically less than half) of the input energy to harmonic frequencies at shorter wavelength. The energy left at the unconverted wavelength(s) remains available for transmission if desired. The excimer lasers (KrF, XeCl, and XeF) are also very good if high pulse energies in the UV are desired. The ruby laser has a slower maximum pulse rate and requires more maintenance than Nd:YAG laser, but it may be satisfactory if its wavelength is optimum. The alexandrite laser is also a prime candidate when it can supply a needed wavelength. It can also be tuned to any wavelength within an interval of about 50 nm to optimize the excitation. These lasers offer a variety of excitation wavelengths, but leave gaps in the 400–500 nm and 550–650 nm regions.

One method of producing excitation within these gaps or at other wavelengths uses a dye laser. Dye lasers that are pumped by flashlamps and Q-switched to form short pulses could perform adequately, although the pulses are usually somewhat longer than for the other lasers. Dye lasers pumped by excimer or frequency-multiplied Nd:YAG lasers have

shorter pulses, but tend to have less pulse energy because of the inefficiency in the tandem lasing.

Other methods are available to produce pulsed excitation at desired wavelengths. For instance, a Raman shifter can convert part of a laser's energy to longer wavelengths with efficiencies as great as 35%. These methods that make a number of other wavelengths possible do so at the cost of increased complexity and less pulse energy.

A satisfactory laser can be found to match quite well any excitation spectrum in the near UV or visible. However, the laser specifications and tracer efficiencies must be considered in combination to design the most effective lidar-tracer system.

4.2 Transmitter, Atmospheric, and Receiver Optics

The transmitter and receiver optics must operate in unison. The transmitted pulses must be aligned within the receiver's field of view, which should be larger than the beam divergence in order to capture all the fluorescence. Collimating or expanding optics may be needed to produce the optimum divergence of the laser output. Small divergence improves the SNR when background light is present, but large divergence can permit eyesafe transmission at higher pulse energies. It may be necessary to block any laser wavelengths that are generated but not used for excitation. This would increase the margin of eye safety and reduce problems of elastic scatter leaking into the fluorescence channels in the receiver. A high optical throughput is desirable because the fluorescent signals are weak.

A pointing or scanning capability is an important feature in a surface-based FT lidar. Three methods are available to maintain alignment between transmitter and receiver. The lasers can be mounted on the telescope and the entire assembly moved in unison. Or, the lasers can remain fixed and their radiation directed through coudé optics. Finally, flat mirrors in a scanner assembly can direct the radiation from fixed lasers outward to the atmosphere and the return signal back to a stationary telescope. Each method is straightforward and has been used in single-wavelength lasers. Careful consideration should be given to find the best configuration if a multiple-FT lidar has several lasers and receiver channels.

Extinction in the atmosphere is a complicating factor in the lidar system. Absorption and scatter by gases and aerosol particles is wavelength dependent and often variable in time and space (Zuev, 1976; Collis and Russell, 1976). Rayleigh scattering by the atmospheric gases increases approximately as λ^{-4}, but spatially is relatively uniform, changing only gradually in the vertical. Extinction by aerosol particles is highly variable in time and space. The wavelength dependence of aerosol extinction is also variable, but is commonly about λ^{-1}. Clouds (except cirrus) are optically dense and effectively block lidar penetration for distances as short as hundreds or even tens of meters. Line absorption by O_2 and H_2O at wavelengths greater than about 600 nm should be considered in lidar design. Continuum absorption by O_3 is large at wavelengths less than about 300 nm. Atmospheric attenuation can lower the SNR and complicate the calibration of the fluorescent signal.

Corrections for atmospheric attenuation can be made when important. An accurate correction for Rayleigh scatter from the atmospheric gases is straightforward and can be

based on simple measurements of pressure and temperature. Correcting for gaseous absorption requires a determination of species concentration, temperature, and pressure. The great variability in concentration and optical properties of aerosol particles makes precise correction for their attenuation difficult. Measurements of elastic backscatter, and perhaps gradients in the profiles of Raman scatter from N_2 or O_2, can provide factors to correct for aerosol attenuation. The degree of attenuation for most FT measurements will not be large, because the maximum ranges will usually be only a few kilometers.

4.3 Optical filtering

Optical filtering in the receiver must separate the received radiation into appropriate passbands for detection. Desired features are high throughput within the passband and adequate rejection of light outside the passband.

Leakage of the strong elastic scatter from the air can be a problem (Kyle et al., 1982). Care must be taken that none of the optical components in the lidar exhibit fluorescence (Rowland and Konrad, 1979b; Kyle et al., 1982). Precautions should also be made to avoid contaminating optical components within the lidar with tracer material.

An interference filter in front of each detector is one optical filtering method. Beam splitters, possibly dichroic, are required to divide the received radiation between the receivers. This is an excellent method for a small number of receiver channels. The filters' transmission curves can be found to good accuracy. However, as the number of channels increases, the mechanical complexity increases and the throughput for each channel declines.

A promising alternative for the multiple-FT lidar is a grating spectrometer, perhaps with a fiber optic directing light to each detector. A spectrometer also offers much more flexibility than interference filters for changing optical passbands. Relative calibration between channels is made easier. However, stray light must be held low enough to avoid leakage of elastic scatter into the fluorescence channels. The design must also account for the presence of higher-order reflections from the grating. Future research should include an evaluation of the performance of a spectrometer compared with interference filters.

4.4 Detectors

Jacobs (1978) described the two types of detectors suitable for the FT lidar. Photomultipliers are best for UV and visible wavelengths. They have fast and linear response, and the dynode gain provides large and almost noise-free amplification. The quantum efficiency depends on the cathode's photoemissive material and on wavelength, but ranges from 30% in the UV to less than 5% for wavelengths greater than 700 nm.

Avalanche silicon photodiodes are usually the best detectors in lidars operating at wavelengths longer than about 900 nm. Their active area must be quite small ($\sim$1 mm^2) for fast response, whereas that of photomultipliers is typically 1–10 cm^2. The small area places a limit on the product of the receiver field of view and aperture diameter. The

photodiode quantum efficiency near 1 μm wavelength is high (even exceeding 50%), but the avalanche gain is much less than in photomultipliers. Avalanche photodiodes are less sensitive to weak signals than photomultipliers with comparably good quantum efficiency.

4.5 Data Acquisition

An analog/digital convertor on the output of each detector changes the signal into a computer-compatible format. The dynamic range of lidar signals is large, which suggests a 10- or 12-bit convertor or else a logarithmic amplifier for dynamic compression before digitization. Since optical signals may sometimes be very weak, an ability to switch to photon counting in such circumstances would provide more accurate measurements.

The data acquisition computer will have several tasks. The essential tasks are ingestion of data, formatting for output, and storage. Some processing and display of data for quality control and experimental guidance are also highly desirable.

5. SUGGESTED LASER-TRACER COMBINATIONS

5.1 One-Tracer System

The Fire Orange FT excited at 532 nm by a frequency-doubled Nd:YAG laser, which is the combination used by Rowland and Konrad (1979b) and by Uthe et al. (1985), remains a very attractive scheme for a single-FT system. The fluorescence efficiency of this FT is the highest among this manufacturer's pigments. This type of laser can produce substantial energy at convenient pulse repetition rates. Robust models of the laser, well suited to field operation, are available. Low-noise photomultiplier detectors can operate in the emission band, although quantum efficiency is only about 10%. A survey of similar orange FTs from other manufacturers may identify a yet better tracer. It may also be possible for a pigment manufacturer to optimize an FT for higher efficiency in the FT lidar application.

The BG cells excited at 248 nm by a KrF laser have potential as an alternative. However, the length of time an airborne cell can maintain its fluorescent efficiency must be determined. The effects of atmospheric absorption and interference from Raman scatter and background fluorescence (see Sec. 6) at these short wavelengths also require examination.

5.2 Two-Tracer System

5.2.1 Principal emission

One attractive two-tracer system consists of Fire Orange excited at 532 nm and either Horizon Blue or Invisible Blue excited by the same Nd:YAG laser frequency tripled to 355 nm. The principal emission spectra are shown in Fig. 15. Horizon Blue looks blue

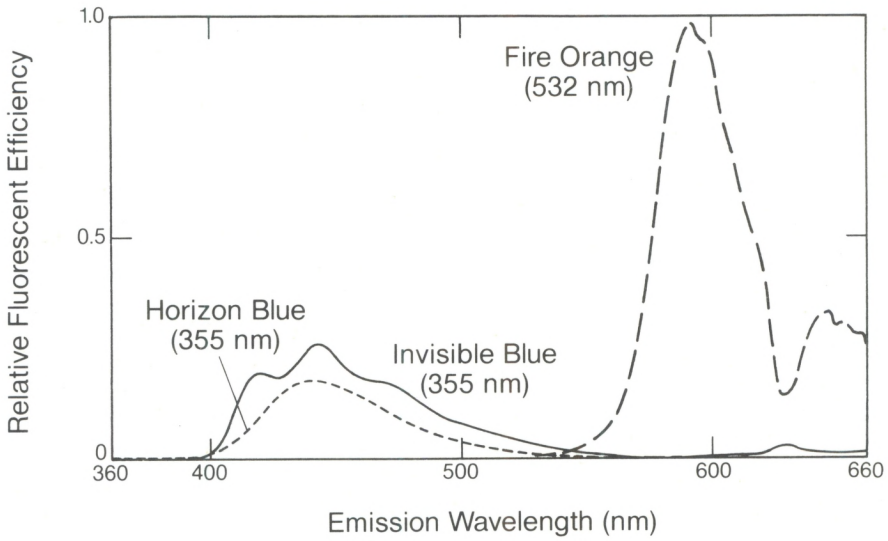

Figure 15. Characteristic principal emission spectra for a two-tracer FP system using the excitation wavelengths shown. Curves are based on 90° emission data (Figs. 3, 4, and 7). Either Invisible Blue or Horizon Blue could be used depending on tradeoffs between efficiency and crosstalk.

under normal light, but Invisible Blue looks white. The "blue" tracers are less efficiently detected than Fire Orange because their fluorescent efficiency is lower and laser pulse energy at 355 nm is less, although photomultiplier quantum efficiency is more than 2 times better.

5.2.2 Crosstalk

The choice between the two "blue" FTs depends mainly on a preference for the higher fluorescent efficiency of Invisible Blue or less crosstalk from the Horizon Blue. Figure 16 illustrates the cross-interference for Invisible Blue and Fire Orange, typical of any two-tracer system when the two exciting wavelengths are transmitted superimposed. The thick solid lines show the two principal modes for excitation and emission. The thin solid line shows the harmless (even helpful) excitation of Fire Orange at 355 nm with emission in the Fire Orange detection band. Emission by an FT within its principal detection band, even when excited by a nonprincipal wavelength, does not compromise the lidar's ability to discriminate between tracers; it can even improve the SNR.

Three more problematic crosstalk modes are shown by dashed lines in Fig. 16. One mode is excitation of Fire Orange at 355 nm and emission in the passband for Invisible Blue. The second mode is excitation of Invisible Blue at 355 nm and emission in the passband for Fire Orange. The third mode consists of excitation of Invisible Blue at 532 nm and emission in the passband for Fire Orange. Note that there is no crosstalk from Fire Orange excited at 532 nm, because fluorescence does not shift emission into shorter wavelengths. These modes complicate discrimination of the tracers, because each detector sees emission from more than one tracer.

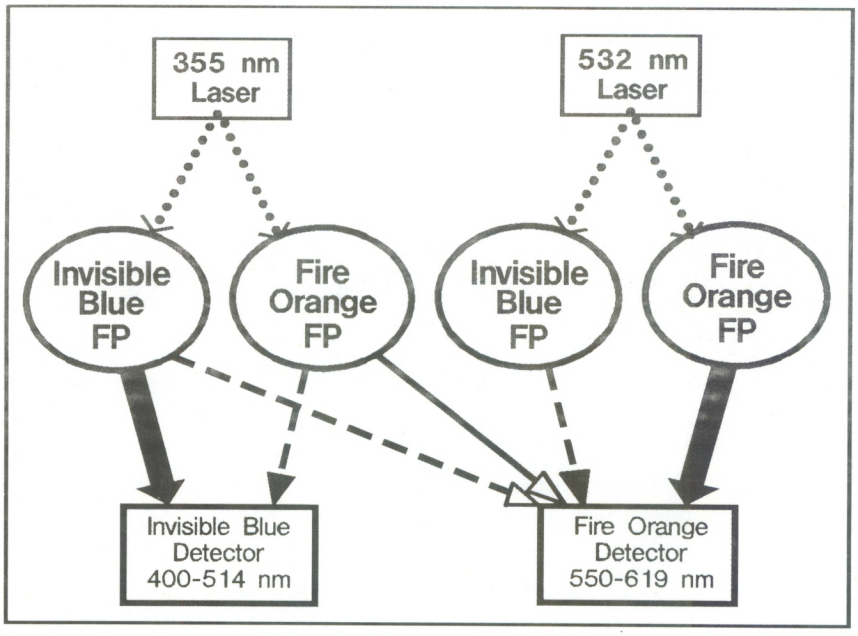

Figure 16. Optical paths from laser to detectors for an example two-tracer system. Principal (solid wide) and secondary (solid narrow) paths provide useful signal. Of the crosstalk (dashed) paths, two with open arrow heads disappear when excitation wavelengths are not superimposed.

An example of the relative magnitude of crosstalk is given in Fig. 17, where our data on 90° fluorescence are used. The tracer concentrations are assumed equal and the lidar sensitivity constant at all wavelengths involved. Unlike the displays of data in Figs. 3 and 7 where questionable data were edited, this simple crosstalk analysis uses data as obtained. Crosstalk amounts below about 2×10^{-2} in Figs. 17 and 19 are at the limit of instrument accuracy and subject to considerable error.

The Fire Orange blend has one fluorophore designed to cascade short wavelengths to the excitation band of the orange-emitting fluorophore (S. Streitel; Day-Glo Color Corp., Cleveland, Ohio; personal communication, 1988). Removal of this ingredient should reduce the crosstalk from Fire Orange excited at 355 nm emitting into the Horizon Blue passband. In any event, Fig. 17 shows that crosstalk with these two tracers is minor.

The crosstalk relationships can be altered by not superimposing the exciting wavelengths, either by pulsing at different times or by transmitting in slightly different directions. The crosstalk paths in Fig. 16 with open arrow heads then disappear. The same paths in Fig. 17 are marked with asterisks. However, separation does not necessarily improve the system. The remaining crosstalk signals become more difficult to quantify because the tracer concentrations are not measured simultaneously. Whether separated or superimposed excitation provides more accurate tracer discrimination depends on the relative magnitude of the crosstalk paths and the variability of tracer concentrations between measurements.

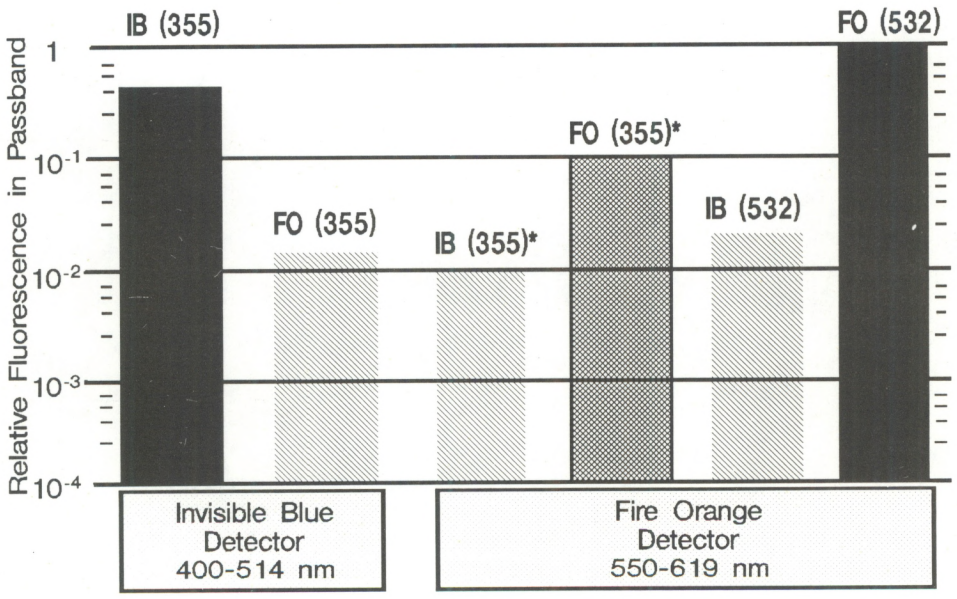

Figure 17. Relative fluorescent efficiencies based on 90° data (Figs. 3 and 7) within the given optical passbands. Contributions are principal (solid), secondary (cross-hatched) and from crosstalk (hatched); those with asteriks disappear if excitation wavelengths are not superimposed.

5.2.3 Other possibilities

Depending on further testing, the BG cells excited at 248 nm and Fire Orange excited at 532 nm might be an excellent two-tracer combination. A disadvantage would be the need for two separate laser systems. The potential advantages are high sensitivity and less crosstalk than would occur with a "blue" FT and Fire Orange.

5.3 Three-Tracer System

The principal emission spectra for a three-tracer system consisting entirely of fluorescent pigments appear in Fig. 18. A frequency-tripled and -doubled Nd:YAG laser excites the Horizon Blue and Fire Orange, respectively. A dye laser could be tuned to the most efficient excitation wavelength near 472 nm for the Saturn Yellow FTs. The detection passbands must be narrower than in the two-tracer case to minimize crosstalk and to avoid any elastic scatter in or near a passband.

The number of possible paths for crosstalk increases rapidly with the number of tracers, as can be seen in Fig. 19. The amount of crosstalk compared with the principal emission is also larger in some paths for the three tracers than for two tracers. In particular, the emission of Horizon Blue excited at 355 nm into Saturn Yellow's passband is not quite a factor of 10 less than the principal Saturn Yellow emission. However, matrix methods (Sec. 7) can be used to solve for the concentration of each tracer.

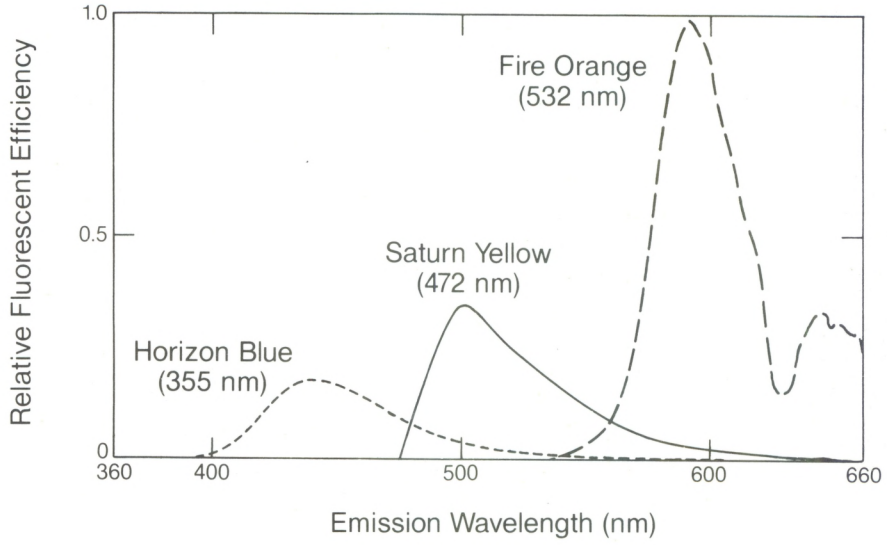

Figure 18. Characteristic principal emission spectra for a three-tracer FT system using the excitation wavelengths shown. Curves are based on 90° emission data (Figs. 3, 5, and 7).

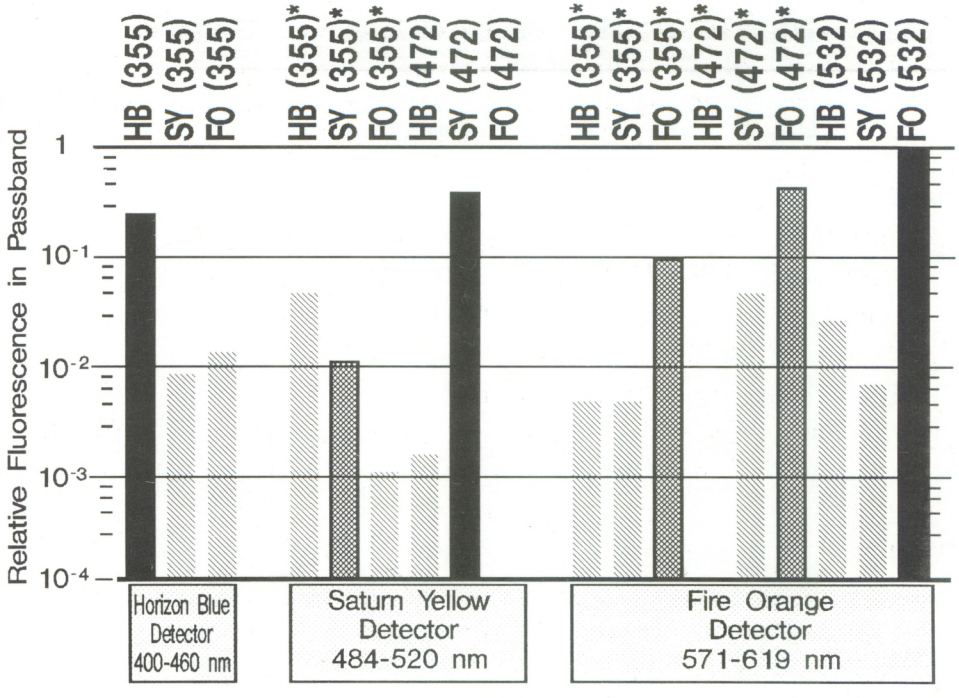

Figure 19. Relative fluorescent efficiencies based on 90° data (Figs. 3, 5, and 7) within the given optical passbands. Shading is as in Fig. 17.

If the BG cells excited at 248 nm prove to be a good tracer and do not emit in the visible, then that tracer added to the Invisible Blue and Fire Orange from the two-tracer system would be attractive. Less crosstalk could result, and still only two lasers would be needed.

6. INTERFERING SIGNALS

The detector signal in an FT lidar can suffer contamination from several sources. The design and signal processing must account for these to optimize the accuracy of the tracer measurements.

6.1 Crosstalk

The presence of overlapping emission spectra in a multiple FT system and the resulting crosstalk are illustrated in Sec. 5. Unless the crosstalk is small enough to be ignored, the processing can obtain the tracer concentrations only through a simultaneous solution of the measurements. This method is described in Sec. 7. The effects of varying degrees of crosstalk in a two-tracer system are evaluated in Sec. 8. It is evident that crosstalk is a fundamental limiting factor for the number of different FTs in a system.

6.2 Raman Scatter

Raman scattering (Inaba, 1976) of laser energy from molecules in the air is downshifted in wavelength and may appear in the FT detection passbands. Although the cross sections for Raman scattering are much smaller than for elastic Rayleigh scattering, sensitive lidar systems can readily detect Raman scatter from N_2 and O_2, which are the main constituents of air. Even water vapor, much lower in concentration, has been profiled by lidar (Melfi and Whiteman, 1985). Previous authors have not considered the effects of Raman scattering on detection of an FT.

The spectrum of Raman-scattered energy from each gas is much narrower than the emission spectrum from an FT. The frequency shift in Raman scattering is independent of the excitation frequency (but the wavelength shift does depend on excitation wavelength). The shift in wavenumber is (Inaba, 1976) 1556, 2331, and 3652 cm^{-1} for O_2 , N_2, and H_2O, respectively. For excitation at 355 nm, these correspond to wavelength shifts of 20.8, 32.0, and 52.9 nm; for excitation at 532 nm the wavelength shifts are 48.0, 75.3, and 128.3 nm, respectively. The Raman cross section varies as λ^{-4}, where λ is the Raman-shifted wavelength, so Raman scatter will be of most concern for FTs emitting in the ultraviolet and blue.

6.3 Background Fluorescence

The amount of fluorescence that may occur from nontracer aerosols and gases is poorly understood. Rowland and Konrad (1979b) interpreted return from ranges close to the lidar as background fluorescence equivalent to Fire Orange loading of about 6×10^{-3}

$\mu g\ m^{-3}$. Uthe et al. (1985a,b) did not mention observation of any background fluorescence from the air. The literature on water vapor profiling with sensitive Raman lidars also does not report any problems with background fluorescence. On the other hand, fluorescence in highly polluted air could be significant (Gelbwachs and Birnbaum, 1973). It appears that background fluorescence will be significant only in highly polluted conditions, but additional research on this matter is desirable.

6.4 Background Light

The consensus of previous research is that daytime background light substantially degrades the sensitivity of a lidar to weak FT concentrations. Fluorescence from the tracer excited by daylight is insignificant in comparison. The effects of background light are considered in detail in Sec. 7 and 8.

6.5 Atmospheric Attenuation

Attenuation of the light on the roundtrip path will modify the level of detected signal. The effects of Rayleigh scatter, most important in the UV and blue regions of the spectrum, can be easily corrected on the basis of air density along the path. Attenuation by aerosol particles is much less predictable. However, approximate corrections can be applied if the optical depth can be estimated from visual observations or from measured elastic backscatter profiles and estimated extinction to backscatter ratio. The maximum range of an FT lidar will usually be a few kilometers or less, so the aerosol attenuation will be minor except in very hazy or polluted air. Attenuation generally will worsen with decreasing wavelength.

Absorption by ozone in the ultraviolet and by water vapor in the red and near IR (Zuev, 1976) could also become significant if overlapped by FT lidar wavelengths.

Clouds or fog in the path will cause severe attenuation and block the FT lidar from useful measurements.

6.6 Detector Noise

Light detectors are quantum detectors, so measurements of weak signals are noisy by nature because of the statistical nature of quantum detection. Thermal noise in photodiodes and the following electronics can also be a factor. The significance of quantum noise on SNR and tracer detection is evaluated in Sec. 8.

6.7 Filter Leakage

The elastic scatter at laser wavelengths can be several orders of magnitude stronger than fluorescence from a diffuse FT. The optical filters on fluorescence channels must be able to reduce the on-line radiation by at least this amount. Kyle et al. (1981) reported difficulty with on-line leakage and also with fluorescence from their dye laser that was

scattered from the atmosphere. Blockage of on-line scatter is a major engineering consideration in an FT lidar.

7. EQUATIONS FOR ANALYSES

Previous authors used measurements (Rowland and Konrad, 1979b; Kyle et al., 1982) and theoretical analysis (Schuster and Kyle, 1980) to evaluate system capability in terms of SIR (signal-to-interference ratio), where signal is fluorescence detected from FTs, and interference is light detected from other sources. They did not explicitly consider the uncertainty introduced by photon statistics (shot noise), nor the ability to detect weak signal in the presence of a large but accurately determined interference. We present equations for the signal from FTs and also from interfering sources. These are in terms of detector photoelectrons within a range gate, from which SIR and SNR are easily calculated. Matrix methods are given to solve for the FT concentrations and to estimate the errors in these concentrations.

7.1 Number of Photoelectrons

We assume a lidar with transmitted pulse fully within the receiver field of view and minimum range much greater than the size ΔR of the range gate. The average number of photoelectrons generated in detector d by fluorescent emission from tracer p excited by laser wavelength λ_l is given by

$$N_{dlp}^{f} = K_l R^{-2} C_p \int B_{lp} T_r F_d \eta_d \lambda \, d\lambda \tag{1}$$

$$K_l = \frac{E_l}{hc} T_{tl} \Delta R A , \tag{2}$$

where f signifies fluorescence, and all quantities in the integrand are in general functions of received wavelength λ. The other parameters are as follows:

R = range
C_p = mass concentration of FT type p
B_{lp} = spectral back-fluorescence cross section of FT type p excited at wavelength λ_l
T_r = transmission from range R to 0
F_d = filter and optics transmission in receiver for detector d
η_d = quantum efficiency of detector d
E_l = pulse energy at wavelength λ_l
h = Planck's constant
c = speed of light
T_{tl} = transmission at λ_l from range 0 to R
ΔR = range resolution (= $c\tau/2$, where τ is sample period)
A = effective area of receiver aperture.

The factor B_{lp}, which can be considered a fluorescent efficiency, is in terms of number of photons emitted divided by the number of photons incident and has units $m^2\ g^{-1}\ sr^{-1}\ nm^{-1}$.

The number of photoelectrons generated in detector d is

$$N_d = M_d + N_d^I , \tag{3}$$

where

$$M_d = \sum_l \sum_p N_{dlp}^f \tag{4}$$

is from the FTs, and

$$N_d^I = \sum_l N_{dl}^R + \sum_l N_{dl}^a + N_d^b + N^d + \sum_l N_{dl}^o \tag{5}$$

is from interfering sources of light. The term N^R in Eq. (5) signifies photoelectrons from Raman scatter, N^a from fluorescence of ambient aerosol particles and trace gases like NO_2, N^b from background light, N^d from dark current, and N^o from leakage of on-line scatter.

Raman scatter from nitrogen (N_2) can be expressed as $N_{dl}^R(N_2)$ and is given by

$$N_{dl}^R(N_2) = K_l\, R^{-2}\, \lambda_l'(N_2)\, [\, \beta_l^R(N_2) T_r\, F_d\, \eta_d\,]_{\lambda_l'(N_2)} , \tag{6}$$

where $\beta_l^R(N_2)$ is the volumetric Raman backscatter coefficient with units of $m^{-1}\ sr^{-1}$, and the parameters in the brackets are evaluated at the shifted wavelength λ_l'. Raman scatter from oxygen (O_2) and from water vapor (H_2O) have similar expressions. The fluorescence from ambient aerosol particles N_{dl}^a is given by an equation like (1), C_pB_{lp} being replaced by C_aB_{la}.

Background light gives

$$N_d^b = \frac{2\,\Delta R}{c}\ \frac{A\,\Omega}{hc} \int L\, F_d\, \eta_d\, \lambda\, d\lambda , \tag{7}$$

where Ω is the solid angle of the receiver field of view, and L is the background irradiance on the receiver. The dark current of a photomultiplier produces

$$N_d^d = \frac{2\,\Delta R}{c}\ \frac{i_d}{q} \tag{8}$$

photoelectrons per range gate, where i_d is the cathode dark current of detector d, and q is the electronic charge. Leakage of on-line scatter of λ_l gives

$$N^o_{dl} = K_l R^{-2} \lambda_l \left[\left(\beta^a_l + \sum_p \beta^o_{lp} \right) T_r F_d \eta_d \right]_{\lambda_l} , \tag{9}$$

where β^a_l is the volumetric backscatter coefficient of ambient molecules and aerosol particles at λ_l, and β^o_{lp} is elastic scatter of laser energy at λ_l from tracer p.

These equations apply to a single lidar pulse. It may sometimes be desirable to average several lidar pulses to improve the effective SNR. Each equation [(1) and (3)–(9)] can be made valid for the sum of photoelectrons from multiple pulses by adding the values on the right-hand side from the pulses. If conditions are constant during n pulses, the multiplicative factor n can be inserted in the right-hand side of these equations.

7.2 Solution for Concentrations

The concentrations of the FT are obtained by first subtracting the interference to obtain the fluorescent signal:

$$M_d = N_d - N^I_d . \tag{10}$$

Note from Eq. (1) that signal from tracer p in detector d from all exciting laser wavelengths can be expressed as

$$\sum_l N^f_{dlp} = G_{dp} C_p . \tag{11}$$

The concentrations and measurements at each range gate then satisfy the matrix equation

$$\mathbf{M} = \mathbf{GC} , \tag{12}$$

where **M** is the vector of the elements M_d, and **C** is the vector of elements C_p. The form of **G** for the system illustrated in Fig. 1 is

$$\mathbf{G} = \begin{bmatrix} G_{11} & 0 & 0 \\ 0 & G_{22} & G_{23} \\ 0 & G_{32} & G_{33} \\ 0 & 0 & G_{43} \end{bmatrix} . \tag{13}$$

In the general case of at least as many detectors as FTs, the concentration vector can be solved (Deutsch, 1965) by

$$\mathbf{C} = (\mathbf{G}^T\mathbf{G})^{-1}\mathbf{G}^T\mathbf{M} , \tag{14}$$

where $\mathbf{G}^T$ and $\mathbf{G}^{-1}$ are the transpose and inverse, respectively, of $\mathbf{G}$. If the number of detectors equals the number of tracers, Eq. (14) reduces to $\mathbf{C} = \mathbf{G}^{-1}\mathbf{M}$. If there are more detectors, the solution to Eq. (14) is in the least-squares sense.

7.3 Noise and Errors

The development thus far considers only the expected number (statistical mean) of photoelectrons. Actual measurements will vary because of photon statistics, calibration errors, and errors in estimating N_d^I, all of which introduce errors to $\mathbf{C}$.

The variance of M_d can be expressed as

$$\sigma^2(M_d) = \sigma^2(N_d) + \epsilon^2(N_d^I) + \Delta_d^2 , \tag{15}$$

where $\sigma^2(N_d)$ is the statistical variance in the number of photoelectrons, $\epsilon^2(N_d^I)$ is the variance in the estimate of the expected value of N_d^I, and Δ_d^2 is the variance in the measurement introduced by the discrete levels in the analog-digital conversion. We neglect Δ_d^2 in the examples to follow, although it can become significant when the dynamic range of the signals becomes large. Since the generation of photoelectrons in period τ is a Poisson random process with variance equal to the mean (RCA, 1974), we have $\sigma^2(N_d) = N_d$.

We also neglect ϵ^2 in Eq. (15), because usually $\epsilon^2 << N_d$ for a well-designed system and measurement program. For instance, N_d^b and N_d^d can be determined to high accuracy for each pulse by recording detector output for many ($\sim 10^2$) range gates before the laser is pulsed (Eberhard and McNice, 1986). The contribution from Raman scatter can be determined where the FT plume is known to be absent. The fraction of on-line scatter leaking into a fluorescent channel can be measured and N_{dl}^o determined by monitoring elastic backscatter with an on-line channel. The fluorescence from ambient aerosol particles will be more difficult to quantify, but should be a factor only when the tracer is very dilute.

All sources of error in Eq. (15) should be evaluated for a particular system. However, the examples given in Sec. 8 show the fundamental limitation to accuracy caused by photon statistics in detecting single or multiple FTs.

The SIR of channel d is defined as

$$(SIR)_d = M_d/N_d^I . \tag{16}$$

The SNR is defined as

$$\begin{aligned}(SNR)_d &= M_d/\sigma(M_d) \\ &\simeq M_d(N_d)^{-1/2} ,\end{aligned} \tag{17}$$

where the approximation is valid when photon statistics dominate. When n pulses are summed, the $(SNR)_d$ has the familiar $n^{-1/2}$ dependence, whereas the $(SIR)_d$ is independent of n.

The propagation of random errors from $\mathbf{M}$ to $\mathbf{C}$ when Eq. (14) is applied can be computed (Deutsch, 1965) from the covariance matrix of expected measurement errors $\mathbf{S}_M$ given by

$$\mathbf{S}_M = < \mathbf{D}_M \mathbf{D}_M^T > , \tag{18}$$

where $\mathbf{D}_M$ is the vector of errors in the measurements and $< >$ means expected value. The covariance matrix of the expected errors in the retrieved concentrations is

$$\begin{aligned}\mathbf{S}_C &= < \mathbf{D}_C \mathbf{D}_C^T > \\ &= (\mathbf{G}^T\mathbf{G})^{-1}\mathbf{G}^T \mathbf{S}_M [(\mathbf{G}^T\mathbf{G})^{-1}\mathbf{G}^T]^T .\end{aligned} \tag{19}$$

$\mathbf{S}_C$ reduces to $\mathbf{G}^{-1}\mathbf{S}_M(\mathbf{G}^{-1})^T$ when the number of detector channels equals the number of tracers.

The diagonal elements in $\mathbf{S}_M$ are the variances given in Eq. (15). The off-diagonal elements are the covariances between detectors, which are zero for photon statistics because the random deviations are independent between detectors. The diagonal elements of $\mathbf{S}_C$ similarly give the variances of the concentration errors. Crosstalk between tracers in any of the optical channels leads to nonzero covariances in the off-diagonal elements of $\mathbf{S}_C$. We use this formalism in sensitivity tests of the number of receiver channels and their optical passbands.

Calibration errors appear as errors in **G**, which lead to errors in **C** in the solution. Unfortunately, the effects of errors from **G** on **C** are more difficult to evaluate than those from **M**, because a straightforward formalism like that in Eq. (19) is not available for errors in **G**. Instead, sensitivity tests must be made for various combinations of **G** and **M** to find the effect of errors in **G**.

The equations presented above can be used to calculate the expected performance of a system, as illustrated in the next section.

8. EXAMPLE SYSTEMS AND THEIR ACCURACY

8.1 Two Independent Tracers

An example of a two-tracer system to illustrate SNR and SIR is shown in Fig. 20. A frequency-multiplied Nd:YAG laser excites Horizon Blue at 355 nm wavelength and Fire Orange at 532 nm, with the beams not superimposed. For these calculations we used the near-180° $B_p(\lambda)$ values from Rowland and Konrad (1979b). The crosstalk is small and is neglected. The accuracies of measured concentrations can then be evaluated separately as if for two single tracers.

The passband of the receiver channel is one lidar parameter that should be optimized. A wider passband gives larger detector signal from the FT. However, interference from background light also increases as the passband widens. (The interference from

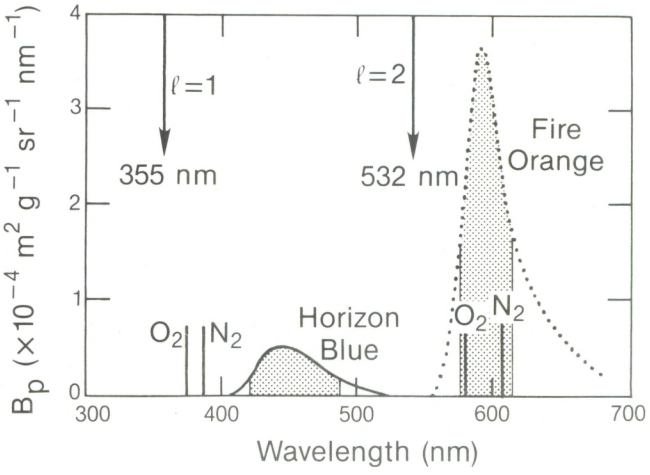

Figure 20. Spectral relationships in a possible two-tracer system. The laser wavelengths are created by frequency-multiplication of a Nd:YAG laser. Emission spectra near 180° (Rowland and Konrad, 1979b) of two commercially available fluorescent pigments are shown; possible receiver passbands are shaded. The wavelengths of Raman scatter from atmospheric N_2 and O_2 are also indicated.

Raman scatter and leakage of on-line scatter also depend on the filter passband.) Figure 21 shows the effect of passband width $\Delta\lambda$ on the SNR for Fire Orange and Horizon Blue where white background light is the only interference. For simplicity, the filter passband was assumed flat with infinitely sharp cutoff at the edges, which were positioned to intercept B_p at equal heights on opposite sides of the peak. The calculated SNR is normalized to that for $\Delta\lambda$ = 100 nm, which is as wide as practical. For no background light (SIR = ∞), Fig. 21 shows little improvement in SNR once $\Delta\lambda$ exceeds 75 nm. In the presence of substantial background light, the optimum $\Delta\lambda$ lies between 50 and 75 nm.

For our evaluation of the system's performance with Fire Orange, we selected a slightly narrower passband (575–615 nm) as a reasonable compromise to help ensure good rejection of on-line scatter in a practical system. The emission band of Horizon Blue is more distant from the 355-nm excitation wavelength, so we selected a wider passband (420–490 nm). Note that Raman scatter from the principal air constituents of N_2 and O_2

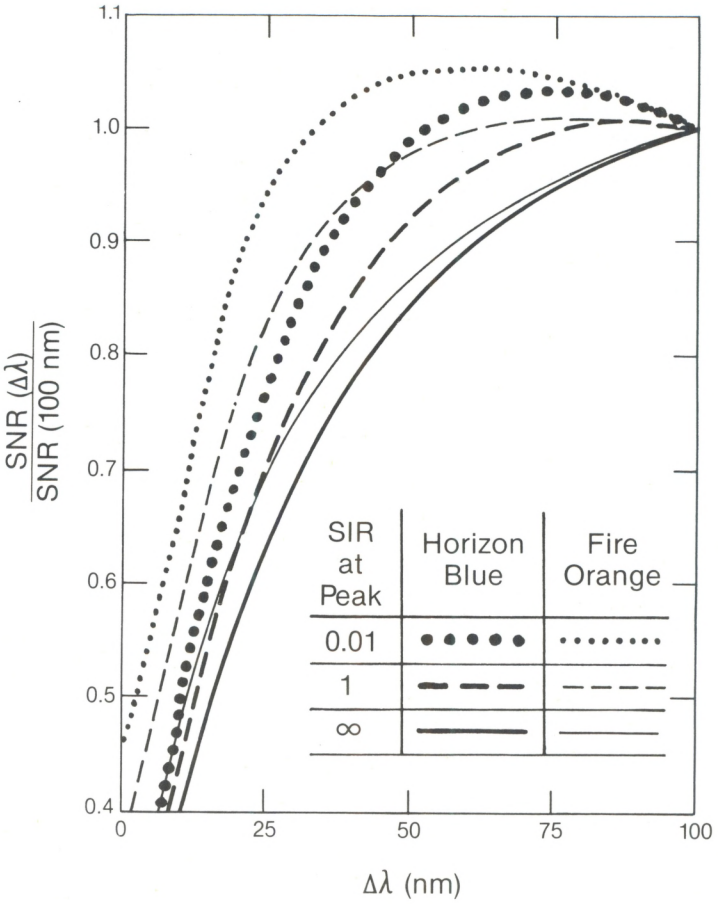

Figure 21. Relative SNRs for detecting fluorescence in the presence of broadband background light as a function of optical passband width $\Delta\lambda$. For "SIR at peak" equal to unity, the spectral irradiance received from the peak of the FP spectrum is equal to the spectral irradiance L of the background light, which is assumed constant over the optical passband. The background is dark when SIR = ∞.

lies within the passband of Fire Orange but outside that of Horizon Blue (Fig. 20). The Raman scatter from H_2O falls outside both passbands.

The signals from the FTs and interfering sources were calculated using the lidar parameters in Table 3. The quantum efficiencies and the value for dark current are typical for an S–20 photocathode. Attenuation by the intervening atmosphere was included by assuming 50–km visual range. In particular, the attenuation coefficient was taken as 0.3, 0.15, 0.1, and 0.075 km^{-1} at 355, 420–490, 532, and 575–615 nm, respectively. The expected performance for the system in Fig. 20 and Table 3 is shown in Figs. 22–24.

The signal levels from the Fire Orange and some sources of interference appear in Fig. 22. The signal decreases linearly with concentration. The decrease with range would be as R^{-2}, except that attenuation by the atmosphere makes the R dependence even stronger. Dark current is negligible in this example. A moonlit cloud produces a photoelectron in only about 1 out of every 30 range gates. A scene brightly lit by the sun generates a strong signal that is comparable with the signal from 10 $\mu g\ m^{-3}$ of the tracer at 0.3–km range. The signal from background light scales linearly with L as can be seen from Eq. (7). The Raman scatter from N_2 and O_2 generates the same signal as a tracer concentration of about 0.1 $\mu g\ m^{-3}$. An FT lidar can encounter a wide range of signal strengths from the tracer or interfering sources.

The scale at the top of Fig. 22 relates plume size and release rate to the plume concentration in the bottom scale. Q ($g\ s^{-1}$) is the release rate, and U ($m\ s^{-1}$) is the mean wind speed advecting the plume. The scale assumes $Q/U = 1\ g\ m^{-1}$ and a uniform distribution of tracer in the cross section of a plume with the area specified. (This can also be

Table 3. Lidar parameters for signal calculations

Parameter	Horizon Blue	Fire Orange
Laser wavelength (nm)	355	532
Pulse energy (mJ)	40	100
Range interval (m)	30	30
Receiver aperture (cm^2)	500	500
Receiver field (mr)	4	4
Optics transmission (%)	20	20
Filter width (nm)	70	40
Quantum efficiency (%)	50	8
Sunlit soil background ($W\ m^{-2}\ sr^{-1}\ nm^{-1}$)	0.045	0.050
Raman scatter:		
N_2 ($10^{-10}\ m^{-1}\ sr^{-1}$)		9.5
O_2 ($10^{-10}\ m^{-1}\ sr^{-1}$)		3.4
Dark current (fA)	2	2

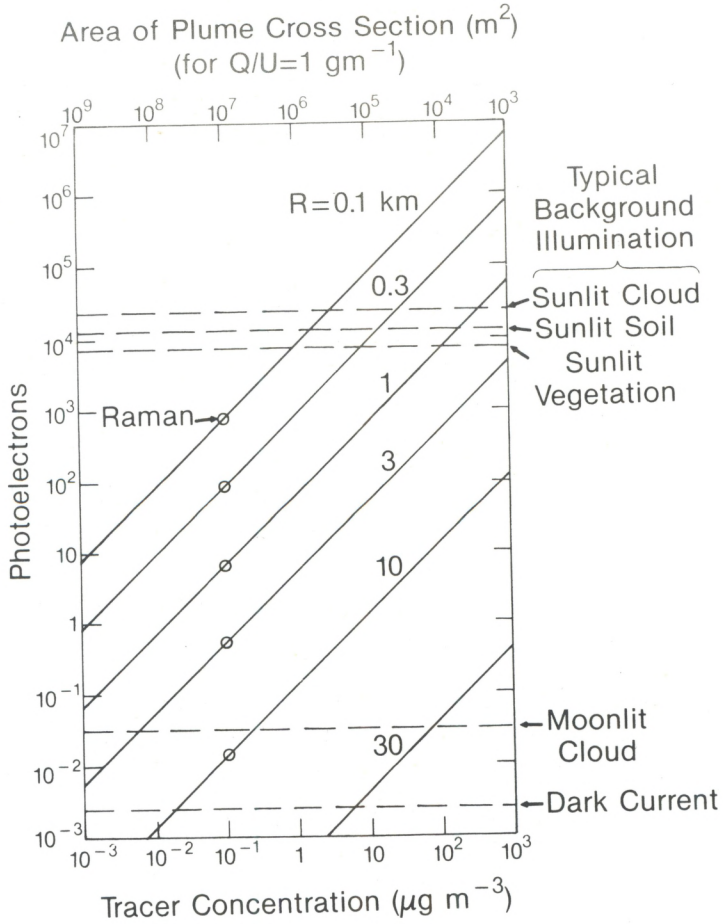

Figure 22. Number of photoelectrons in one range gate as a function of concentration (bottom scale) of Fire Orange particles. Detected fluorescence (solid lines) at several ranges from the lidar; detected Raman scatter (o) from both nitrogen and oxygen; and typical levels (dashed lines) of background light. See Table 3 and Fig. 20 for lidar and tracer parameters. The scale at the top relates plume size to tracer concentration.

interpreted as the characteristic area of a nonuniform plume to obtain a characteristic concentration.) The tracer concentration is proportional to Q/U and inversely proportional to the cross-sectional area. The concentration on the bottom scale corresponds to the value on the top scale found by multiplying the plume's cross-sectional area (in m^2) and the Q/U (in g m^{-1}).

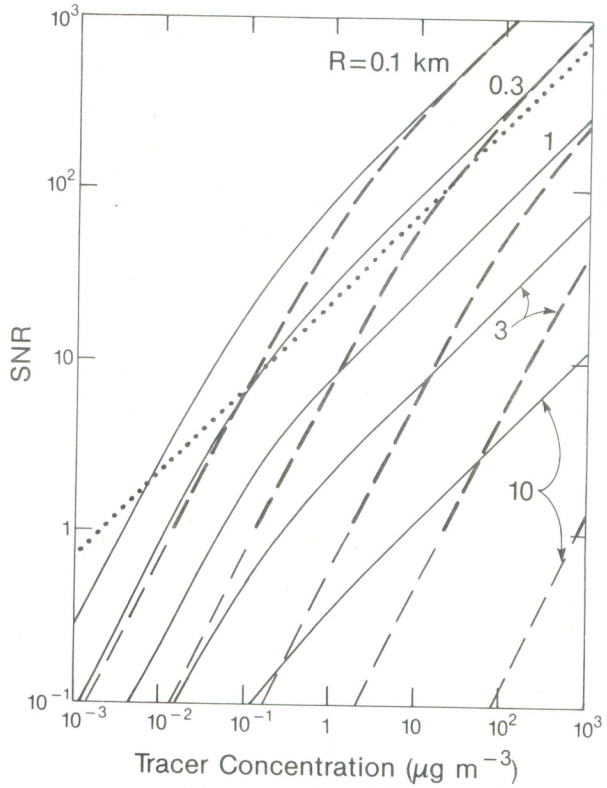

Figure 23. SNR as a function of concentration of Fire Orange particles: No background light (solid lines); sunlit soil in background (dashed lines); and narrower optical passband excluding Raman scatter at 0.3–km range when the background is dark (dotted line). Data are based on Fig. 22. The thinner dashed lines indicate where the background light is at least 100 times greater than the FP signal.

The SNR based on Fig. 22 and calculated from the shot noise approximation in Eq. (17) is given in Fig. 23. For this case of an independent tracer,

$$\sigma(C)/C = (\mathrm{SNR})^{-1}, \tag{20}$$

where C is the true tracer concentration and $\sigma(C)$ is the standard deviation of the random error in C from shot noise. The solid lines are for dark background. The dashed lines show a poorer SNR when the background light is bright, especially for large R. The thin dashed lines indicate where the calculation is not dependable, because the background light is too strong for $\epsilon(N^b)$ to be neglected. Very dilute tracer concentrations, large R, and large L must be avoided to achieve high SNR.

The slopes of the solid lines change at 0.1 μg m^{-3}, below where the Raman scatter is significant. The dotted line shows the effect of narrowing the passband to 20 nm and excluding the Raman scatter for R = 0.3 km and dark background. The narrower passband dramatically improves the SNR at concentrations less than about 0.1 μg m^{-3}, but decreases the SNR by only 22% for somewhat higher concentrations.

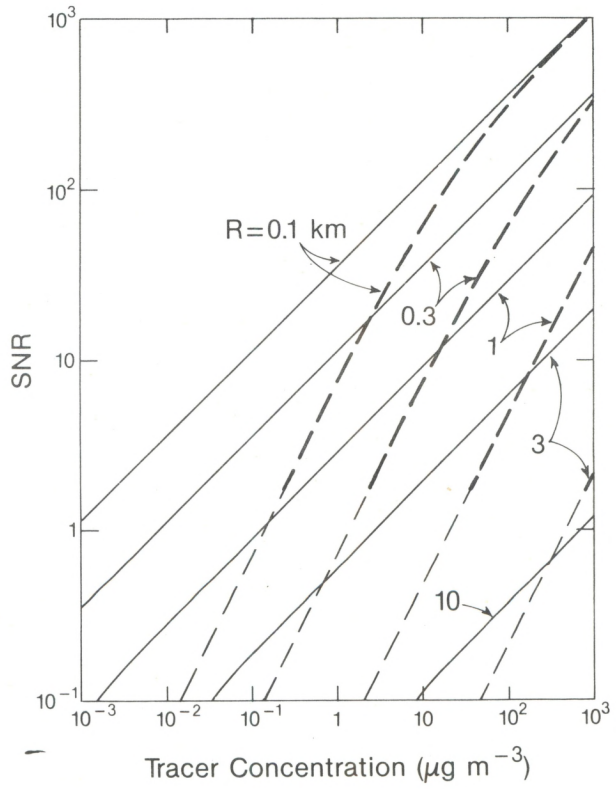

Figure 24. SNR as a function of concentration of Horizon Blue particles (see legend for Fig. 22). Data are based on Table 3 and Fig. 20.

The SNR for Horizon Blue is plotted in Fig. 24. The effects of background light and atmospheric attenuation are greater than for Fire Orange. The absence of Raman interference with the Horizon Blue is an advantage at low concentrations. However, the net effect is lower SNR for Horizon Blue than for Fire Orange.

The practical limits to precision for this system can be illustrated by an example of long-range transport. Assume that an airborne lidar is flown 1 km above the FT plumes at night, U = 10 m s^{-1}, and crosswind plume dimensions are 300 m vertical by 3500 m horizontal. A release rate of Q = 1 g s^{-1} (which would cost about \$50 h^{-1} for the material in each tracer) would make a characteristic concentration of 0.1 μg m^{-3}. The lidar could observe this with an SNR of roughly unity, which is adequate for describing the plume's location, size, and shape. If more accurate concentration data are required, the precision could be increased by averaging data from several range gates or pulses, by improving the lidar's sensitivity, or by releasing more tracer.

On-line backscatter from the molecules and ambient aerosol particles of the atmosphere will usually be much stronger than the FT signal. Typical values of β^a for 50 km visual range are 1.0 × 10^{-5} and 4.0 × 10^{-6} m^{-1} sr^{-1} at 355 and 532 nm, respectively. Without optical filtering, the backscatter at 355 nm will induce signals in the example system equivalent to 3600 and 460 μg m^{-3} of Horizon Blue and Fire Orange, respectively.

The corresponding equivalent concentrations for backscatter at 532 nm happen to be almost identical in this case. If leakage of on-line scatter must remain below 10% of the signal from 10^{-3} μg m^{-3} of FT, the optical filter in each fluorescent channel must have a rejection of at least 3.6×10^6 at 355 nm and 4.6×10^5 at 532 nm. Extra channels that monitor the on-line scatter can provide data for subtracting any on-line signal that has leaked into the fluorescent channel.

Calibration errors in receiver sensitivity or in $B_p(\lambda)$ will also introduce errors into the inferred concentrations. The fractional error in concentration will be in proportion to the fractional calibration error of the corresponding channel. Such errors probably will be biased, unlike the random uncertainty introduced by shot noise.

The Horizon Blue, excited by a frequency-tripled Nd:YAG laser, and Fire Orange, excited by frequency-doubling the same laser, are very attractive for a simple two-tracer system.

8.2 Shot Noise for Two Idealized Tracers With Crosstalk

The effects of shot noise when considerable overlap exists in the emission spectra are illustrated by the two-tracer system in Fig. 25. The spectrum (B_1) of tracer 1 is that of Blaze Orange pigment (Rowland and Konrad, 1979b) excited at 532 nm wavelength, although we had to extrapolate emission data for $\lambda > 675$ nm. The shape of this spectrum is typical of many fluorophores; it has a wider peak than does Fire Orange. Tracer 2 is the identical spectrum, translated to 30–nm–longer wavelength. We chose this somewhat artificial, idealized example as a convenient way to illustrate the important effects of shot noise and calibration errors when crosstalk is present. This degree of overlap is roughly as much as could be tolerated in a practical system.

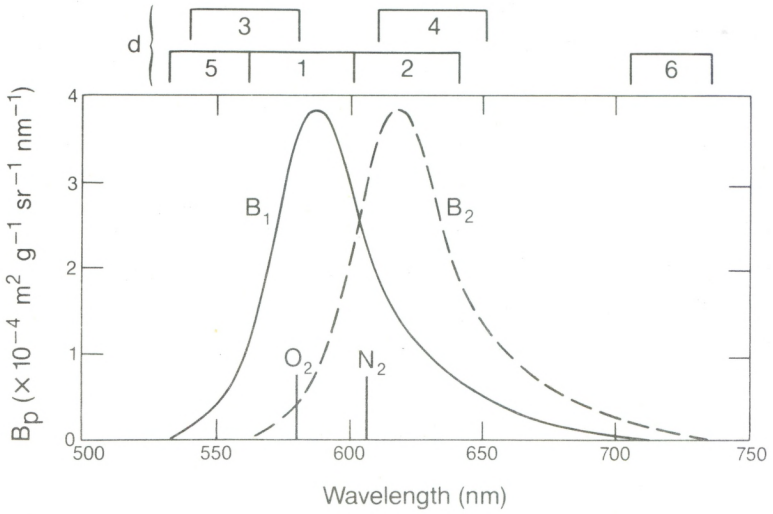

Figure 25. Spectral relationships for illustrating the effects of strong crosstalk. Six possible receiver passbands are shown at the top. Excitation is at 532–nm wavelength.

We evaluate the effectiveness of four different combinations of receiver channels chosen from those shown in Fig. 25. The spectral sensitivity of each channel is flat over the bracketed band of wavelengths. Calculations using Eq. (19) provide the magnitudes of uncertainties that propagate from the shot noise to the solution for C_1 and C_2 from Eq. (14). Lidar system parameters are the same as for Fire Orange (Table I), and we chose a single range of R = 1 km.

In the first combination, channels d = 1 and 2 are centered near the peaks of tracers 1 and 2, respectively. The lidar gain matrix, normalized by the largest principal element G_{22}, is given by

$$\mathbf{G} = G_{22}\begin{bmatrix} 0.955 & 0.233 \\ 0.462 & 1 \end{bmatrix} . \tag{21}$$

The two principal (diagonal) elements are nearly identical. The crosstalk elements are almost 1/4 or 1/2 as large, respectively, or proportionately much worse than any similar terms in Figs. 17 or 19.

Figure 26a shows the typical fractional error in concentration $\sigma(C_1)/C_1$ caused by shot noise. In the absence of the other tracer ($C_2/C_1 = 0$) and with a dark background, the solid line at the bottom shows a decrease in accuracy with decreasing concentration. The curve steepens for C_1 less than about 0.1 μg m^{-3}, where the Raman scatter from O_2 within channel 1 is significant. The bottom dashed line includes the additional degrading effect of background light from sunlit soil. These features are similar to those in Fig. 23, where no overlap exists in the emission spectra.

The main effect of overlapping spectra shown in Fig. 26a is the increase in the uncertainty of C_1 when the other tracer is present ($C_2/C_1 > 0$). When $C_2 >> C_1$, and C_2 is hence the dominant source of shot noise, then $\sigma(C_1)/C_1$ is proportional to $(C_2/C_1)^{-1/2}$. If C_2/C_1 is large, the presence of tracer 2 masks the lidar's ability to observe the more dilute concentration of tracer 1.

The accuracy of C_2 for the same situation is shown in Fig. 26b. The plots are almost identical to those in Fig. 26a, with two exceptions. First, the effect of Raman scatter is stronger, because Raman scatter is stronger from N_2 than from O_2 (Table 3). Second, the presence of C_1 has a slightly larger effect on the accuracy in C_2, because channel 2 receives more signal from tracer 1 than channel 1 receives from tracer 2.

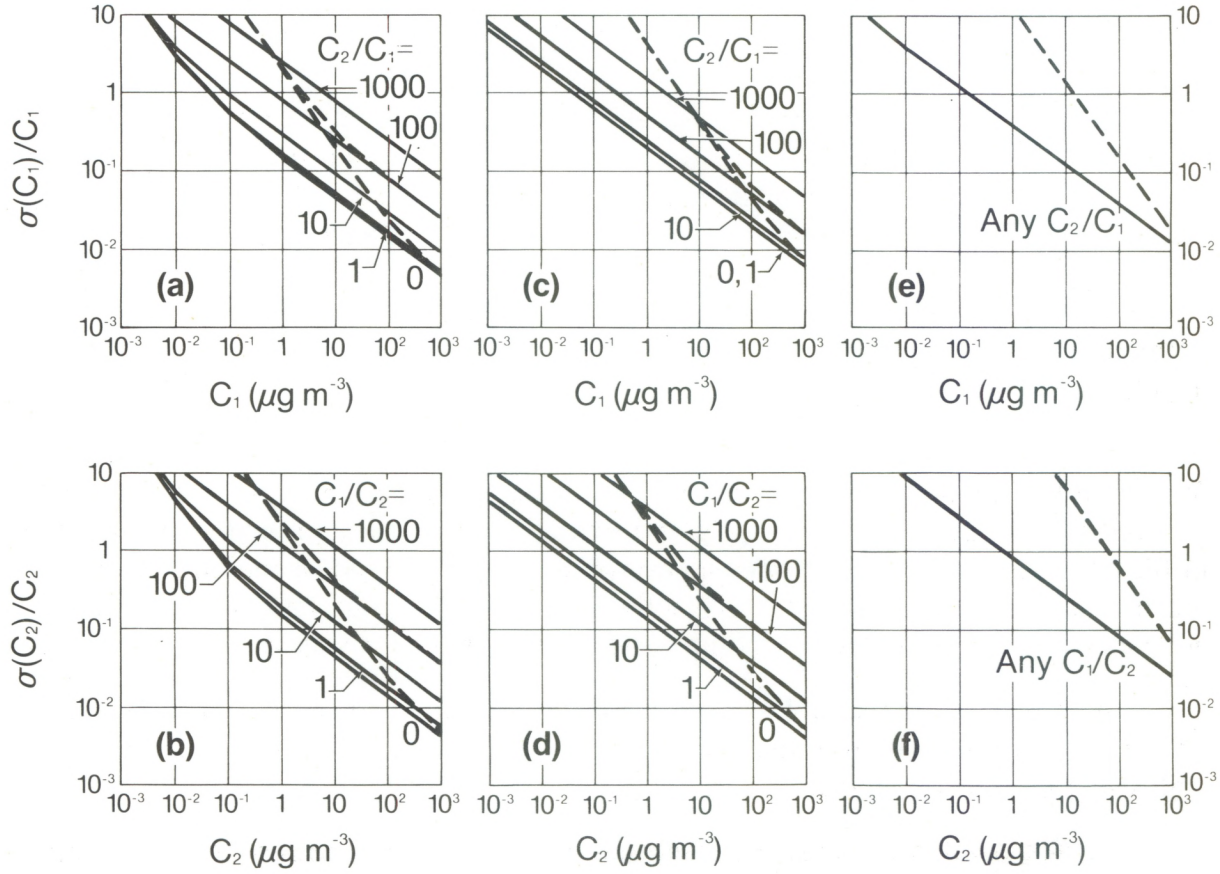

Figure 26. Normalized standard deviation of concentration caused by shot noise, based on data in Fig. 25 and the right-hand column of Table 3: (a)–(b), optical channels d = 1, 2; (c)–(d) d = 3, 4; (e)–(f), d = 5, 6. Solid lines indicate dark background; dashed lines indicate sunlit soil in the background for $C_2/C_1 = 0$, for $C_2/C_1 = 100$ [(a), (c), and (e)], and for $C_1/C_2 = 100$ [(b), (d), and (f)].

The second combination of receiver channels consists of d = 3 and 4 (Fig. 25). These passbands are shifted apart to exclude the Raman signals. The curves of $\sigma(C)/C$ for dark background (solid lines in Figs. 26c and 26d) therefore remain straight, even for tracer concentrations less than 0.1 μg m^{-3}. The matrix normalized by the largest principal element G_{42} is given by

$$\mathbf{G} = G_{42}\begin{bmatrix} 0.431 & 0.025 \\ 0.378 & 1 \end{bmatrix} . \qquad (22)$$

The sensitivity to tracer 1 in channel d = 3 is only 43% of tracer 2 in channel d = 4. Crosstalk of tracer 1 in channel d = 4 is still large, but the crosstalk sensitivity to tracer 2 in channel d = 3 is an order of magnitude smaller.

The shift of the passbands away from the emission peaks reduces the number of FT photons, especially for d = 3. When only one tracer is present, this shift reduces the accuracy in detecting that tracer. This is most apparent in differences in the plots for C_2/C_1 = 0 in Figs. 26c and 26a. Changing from channel 1 to 3 does reduce the crosstalk from tracer 2 even more than the change decreases the contribution from tracer 1. The masking of tracer 1 by tracer 2 for $C_2/C_1 > 10$ in Fig. 26c is therefore considerably smaller than in Fig. 26a. However, changing from channel 4 to channel 2 reduces the masking of tracer 2 by tracer 1 by very little (Fig. 26b and 26d). The background light damages the precision more in Figs. 26c and 26d than in Figs. 26a and 26b. In brief, the combination of d = 3 and 4 is noticeably better than d = 1 and 2 when (1) background light does not dominate the signal and (2) either the tracer concentrations are low enough to make avoidance of Raman scatter desirable or C_2/C_1 is large.

The third combination of receiver channels is d = 5 and 6 (Fig. 25), each of which is 30 nm wide and positioned to remove crosstalk. The FT signals arise from very weak portions of the spectra, especially for tracer 2. The concentration errors from shot noise in Figs. 26e and 26f show no dependence on the concentration of the other tracer. Masking by the other tracer therefore is not a problem. The combination of d = 5,6 is less accurate than the previous two combinations, except for a masked tracer.

The fourth combination has four channels, namely d = 1, 2, 5, and 6. This combination (results not shown) improves the accuracy at most by a disappointing 2% compared with using only d = 1 and 2.

We have evaluated several different situations of using more than two channels for detecting two tracers with crosstalk. The improvement in accuracy in some circumstances can be significant (e.g., 30%). However, the added complexity and the possible loss of optical throughput tend to neutralize the advantage from using more fluorescent channels than tracers.

The experimenter might sometimes know *a priori* that one tracer is absent. Using this knowledge in data processing can improve the accuracy. For example, assume $C_2 = 0$ for the conditions in Fig. 26a. When the signal in channel d = 1 is processed for C_1 as the only tracer, $\sigma(C_1)/C_1$ is about 13% less than if the matrix method is used for two tracers. Alternatively, the signals from both channels 1 and 2 can be summed to form an equivalent channel. This procedure reduces $\sigma(C_1)/C_1$ by an additional 18% when Raman scatter is negligible. When Raman signal is strong, the degree of improvement depends on the relative sensitivity of the two channels to FT and Raman scatter. Setting $C_2 = 0$ reduces $\sigma(C_1)$ by eliminating the possibility of shot noise "creating" positive (or negative) C_2 at the same time the noise is forcing C_1 smaller (or larger). This refinement would be useful wherever the data indicate that atmospheric dispersion has not yet merged the two tracers.

A matrix solution of data that are acquired simultaneously allows discrimination between two FTs that have overlapping emission spectra. All else being equal, the accuracy in concentration is comparable with that of two independent tracers, except for one

major limitation. The combined effect of shot noise and crosstalk will mask one tracer when the other is present in much larger concentration. The severity of the masking will be smaller for spectra with less overlap than the stringent example (Fig. 25) discussed here.

8.3 Calibration Errors for Two Idealized Tracers With Crosstalk

When crosstalk is present, a calibration error can affect more than one tracer. In this section we discuss the biases in concentration caused by two types of errors. We use as an example the two tracers in Fig. 25 as measured by channels $d = 1$ and $d = 2$.

We first simulate an error δG_{21}, which could be caused by an imperfect calibration of the portion of $B_p(\lambda)$ that falls within the passband of $d = 2$. The resulting fractional errors in concentration (e.g., $\delta C_1/C_1$) were determined as follows. The measurements were calculated from Eq. (12) using the correct matrix **G**. The solution for erroneous concentrations, such as $C_1' = C_1 + \delta C_1$, were found from Eq. (14) by replacing **G** with **G'**, where $G_{21}' = G_{21} + \delta G_{21}$.

The error δG_{21} is positive when B_1 within $d = 2$ is believed to be larger than it actually is. The corresponding δC_2 is negative (Fig. 27), and δC_1 is positive (Fig. 27a).

When C_1 is dilute compared with C_2, the error in G_{21} has negligible effect on the inferred C_2. In the opposite case of small C_2/C_1, the fractional error in C_2 is significant (in this example about half $\delta G_{21}/G_{21}$). Figure 27a shows that the errors in concentration depend on C_1 and on the fractional error in G_{21} but are independent of C_2. The error in C_1 in Fig. 27a is about five times smaller than the error in C_2. Although not shown in Fig. 27, the magnitudes of the concentration errors decrease as G_{21}/G_{11} and G_{21}/G_{22} become smaller.

The second simulation considers an error in the sensitivity of channel 2, when $\delta G_{21}/G_{21} = \delta G_{22}/G_{22}$. Positive values mean that the channel is believed to be more sensitive than it actually is. A positive calibration error makes (Fig. 28) C_2' too small and C_1' too large. The errors in concentration depend on the fractional calibration error, on C_2/C_1, and on the relative magnitudes of the elements in **G**. Tracer 2 is affected more than tracer 1. When one tracer is dilute compared with the other, the fractional error in the dilute FT can be very large. This error is not without bound, because normalizing δC_1 and δC_2 by $C_1 + C_2$ (Fig. 29) reveals a dependence on the concentration of the denser tracer. Although the fractional error in the denser tracer is much smaller, it can still be significant. When the two tracers have roughly equal concentrations, the errors are less troublesome.

These are two examples of relative calibration errors that distort the ratio of the elements of **G** in the presence of crosstalk. Such errors often change the concentration inferred for one tracer at the expense of the other. The resulting errors in concentration are a complicated function of the calibration errors, the relative magnitudes of the matrix elements in **G**, and the ratio of the concentrations of the two tracers. The fractional errors in concentration can be serious. When one tracer is much denser than the other, calibra-

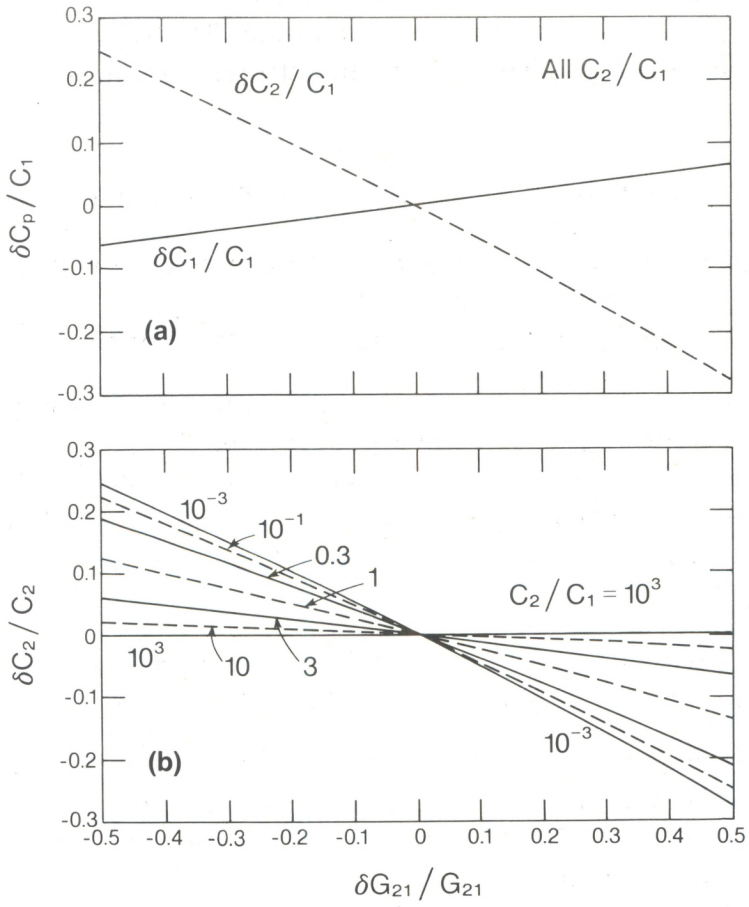

Figure 27. Normalized errors in concentrations caused by a calibration error for B_1 within receiver channel $d = 2$ (Fig. 25): (a) δC_1 and δC_2 normalized by C_1; (b) δC_2 normalized by C_2.

tion errors can destroy the measurement accuracy of the more dilute tracer. Intercalibration must be precise whenever emission spectra overlap and cause crosstalk. Of course, better separation of the emission spectra will decrease the crosstalk and reduce the severity of this problem.

9. CALIBRATION PROCEDURES

Several schemes for calibrating an FT lidar are available that vary in accuracy and difficulty. The selection depends on the degree of error in tracer concentrations that can be tolerated, balanced against the resources required for calibration. More than one calibration method with as much independence as possible is desirable, especially during the development phase of FT lidar.

A lidar's spatial and temporal coverage of the distribution of a tracer can temper the need for accurate calibrations in many applications. For example, the position, size, and shape of a plume or puffs of tracers give valuable information, even without any amplitude calibration, as demonstrated by Uthe et al. (1985b) for a single FT.

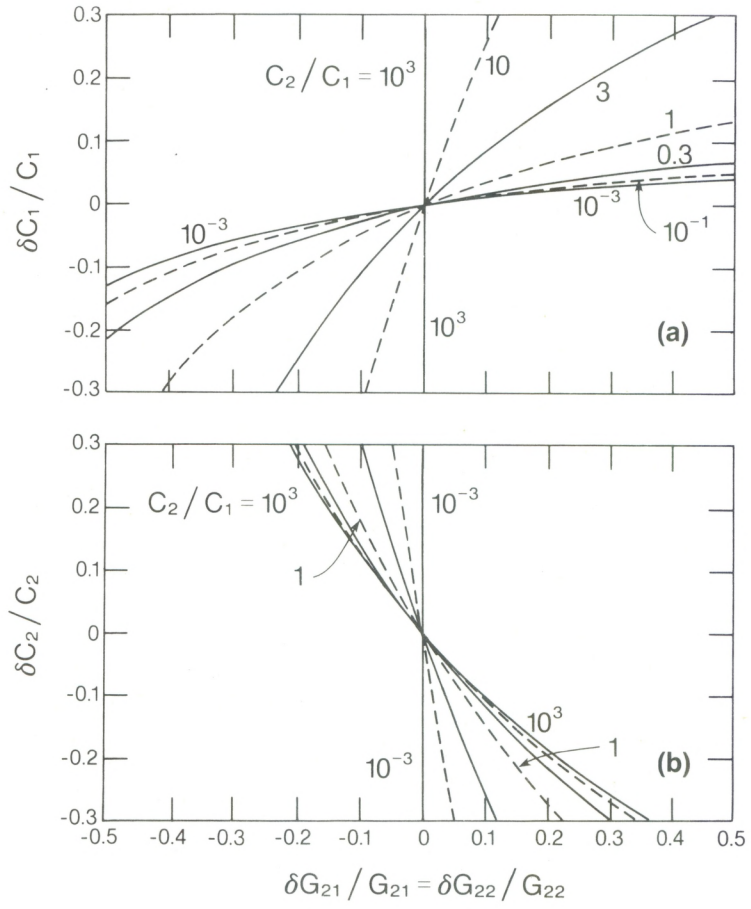

Figure 28. Fractional errors in concentrations caused by a calibration error for channel $d = 2$ (Fig. 25). The family of C_2/C_1 is the same as in Fig. 27.

Calibration of a multiple-FT lidar will be more important, especially in terms of concentration ratios between tracers. First, good discrimination between FTs with crosstalk implies accurate measurement of their concentration ratio. Second, the multiple-FT lidar will probably be applied to problems in which the ratio is an important result, especially if atmospheric diffusion mixes the tracers in the same air mass. In any event, calibration methods suited to particular applications need to be made available.

Calibration of an FT lidar faces several difficulties. The performance of some of the components may not be constant. The laser, interference filters, and detector may degrade with use. The calibration includes the integral of the spectral product of the filter passband with the emission spectrum, which can be time-consuming to measure. The lidar's geometry of 180° fluorescence from an ensemble of individual FPs is difficult to duplicate in the laboratory. A final problem is that constancy of fluorescence efficiency per unit mass, which depends on manufacturing, size distribution, and degree of clumping, has not been verified for any tracer. Calibration procedures should deal with these uncertainties.

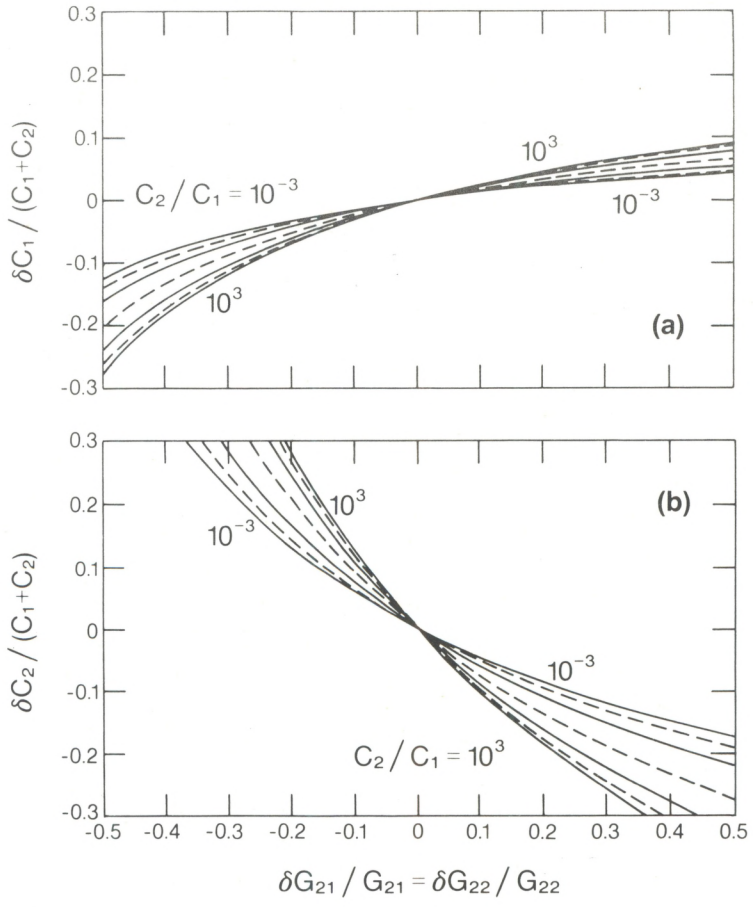

Figure 29. Fractional errors in concentrations, as in Fig. 28, but errors are normalized by $C_1 + C_2$.

9.1 Laboratory Component and Subsystem Measurements

The optical or electronic properties of individual components can be measured and the overall lidar performance calculated from the data. Such measurements, or perhaps manufacturer's specifications for some components, are needed during the design and construction of a lidar. However, a precise calibration with this method will be very difficult because of accumulated errors. Also, duplication of the spatial and spectral distribution of energy through all components individually requires a heroic laboratory effort. Imitation of field conditions can pose considerable challenges in laboratory calibrations.

This approach can be more useful for calibration of subsystems, such as the receiver assembly past the focal plane of the telescope.

Laser pulse energies are very likely to fluctuate a few percent, or even tens of percent, in the short term, especially in field conditions. An energy monitor for each transmitted wavelength is desirable for calibrated operation.

9.2 Raman Scatter

Raman scatter from N_2 or O_2 molecules can be part of the calibration strategy for a highly sensitive FT lidar. Raman scatter from H_2O is less suitable because the signal is weaker and varies with absolute humidity. Raman scatter will provide a complete system calibration for the excitation wavelength and the particular Raman wavelength(s) within a receiver passband. However, this method does not calibrate over the entire passband, nor does it calibrate the fluorescence efficiency of the FT, which could be obtained by laboratory or special field measurements. By interchanging filters, one could remove almost all relative error between spectrally adjacent channels. Raman scatter from air void of FTs and with negligible background fluorescence is an excellent method to monitor any changes in laser output, optics transmission, and detector sensitivity.

9.3 Calibration Target

A diffusely scattering target that intercepts the entire laser beam is one common technique for calibrating lidars for elastic scatter. The target's 180° reflectivity must be determined separately. The signal from the target is very strong, so optical or electronic attenuation is required to bring the lidar within the normal operating range for atmospheric signals. This method could be extended to an FT lidar if a target could be constructed that adequately mimic the FTs. However, a paint or coating of an FT on a flat surface may suffer self-absorption that can alter the emission spectrum from that of airborne particles. Hard target calibration for an FT lidar has not been attempted before, but warrants investigation.

9.4 Plume Flux

The plume flux technique used by Eberhard et al. (1987) is excellent for calibration when it can be accomplished. A continuous release at rate Q into a wind of measured speed U forms a plume. The lidar scans across the plume to obtain the integrated tracer signal projected on a plane normal to the plume axis. Repeated scans are often necessary to average out the "lumpiness" in concentration created by turbulence. In the simple case of a single tracer the range-corrected detector signal is defined as

$$m = MR^2T_tT_r \tag{23}$$

where M is the detector signal, R is range, T_t is atmospheric transmission of the laser light, and T_r is the effective atmospheric transmission of the fluorescence on the return path. Assuming a conservative tracer, the concentration C from a measurement m anywhere in the plume is given by

$$C = m\ Q/U\ m^{yz} \tag{24}$$

where m^{yz} is the average cross-sectional integral of signal. Although special experiment arrangements may be needed to apply the plume flux method, it is the only one that directly calibrates the entire FT lidar system, including tracer fluorescence efficiency at 180° and any dependence on how the tracer is dispensed.

9.5 Comparison With Standard Tracers

Comparison of lidar-measured FT concentrations with those of another tracer is the most independent method. It could be used to calibrate the lidar initially, but perhaps is better reserved for validation of other calibration procedures (e.g., Eberhard et al., 1987). The tracer releases must be simultaneous and colocated. Sampling should also be synchronized, even though point sampling of a gas like SF_6 for comparison with the above-ground lidar measurements can present some experimental challenges.

9.6 Interference and Crosstalk Checks

Any tracer experiment should include measurements of background levels and checks for interfering signals. A lidar could perform these tests upwind of release, before release begins, or in regions vertically or horizontally removed from the tracer.

The presence or suspicion of crosstalk in a multiple-FT lidar calls for an analogous check to fine-tune the nonprincipal elements in **G** (nondiagonal elements if the matrix is square). Taking each tracer in turn, lidar data should be acquired in all receiver channels when none of the other tracers is present. The relative magnitudes of the matrix elements can then be adjusted to yield zero concentrations of the absent tracers for the test data. During regular measurements this procedure should substantially restrict the kinds of errors shown in Figs. 27–29.

10. COMPARISON WITH OTHER TRACER METHODS

10.1 Other FT Detection Methods

Two *in situ* techniques for detecting FPs have been demonstrated that could be used in combination with lidar remote sensing of FTs.

First is the approach described by Leighton et al. (1965) and summarized in the Introduction. The tracers could be collected on filters or by impaction devices and analyzed under appropriate illumination in the laboratory for FP concentrations. This might be a valuable way to measure FTs at the surface where the lidar is blocked or data are contaminated by ground strikes. This method also is useful for time-average sampling at a point in contrast to the lidar obtaining "snapshots" of distributions over a large area.

The second method uses a sensitive optical particle counter modified for fluorescence detection (H. Halstead, Dept. of Atmospheric Sciences, University of Washington, Seattle, Washington; personal communication, 1988). The sampled air stream flows

through the beam of a CW laser. A long-pass optical filter in front of a photomultiplier blocks the elastically scattered light but passes the fluorescent emission. A thresholded pulse-height analyzer was able to detect FPs with diameters as small as 0.1 μm with no noise counts and no false counts from much larger, nonfluorescent particles. Halstead has suggested a two-tracer FP counter with two detectors preceded by filters with different cutoff wavelengths.

10.2 Other Tracers

Various gases, such as SF_6 and perfluorocarbon (Johnson, 1983), have been widely used as tracers in studies of atmospheric transport and dispersion. Bag or syringe samples are usually gathered *in situ* at a number of points in the experiment area, usually with some averaging in time. The concentration of tracer in each sample is determined later in the laboratory by gas chromatography or other analytic procedure, although real-time sensors are now available for some gases. Lidar sensing of tracers has complementary characteristics. Measurements are made remotely, and approximate concentration data are readily available in real time. A lidar is best suited to revealing the morphology of the elevated portion of a plume; ground strikes contaminate data very near the surface. Although the gas tracer methods probably are more accurate, an FT lidar can provide a much more comprehensive description of the fate of a tracer.

Lidar can sense elastic scatter from tracer particles like power plant ash or oil fog (Johnson, 1983; Eberhard et al., 1987) with good SNR. However, the rather high and variable amount of ambient aerosol particles limits dependable measurements at large distances from the source. In particular, any other strong sources of aerosol particles can confuse the signal. A major asset of the FT lidar is low background fluorescence, so much lower concentrations can be detected.

Lidars using DIAL (DIfferential Absorption of Light) are able to detect concentrations of some pollutant gases (Collis and Russell, 1976), such as SO_2, NO_2, and O_3; H_2O can be measured with DIAL or Raman techniques. These gases can be used as tracers of opportunity in some applications. However, DIAL and Raman measurements often require extensive pulse averaging for adequate detection because the innate sensitivity is poor. The amount of gas required is generally too high for practical use as an artificial tracer. The SNR calculations in Sec. 8 indicate that the practical sensitivity of FT lidar will be on the order of 1 ppb (by mass) in air for one pulse and 30 m range resolution. This FT sensitivity is significantly better than the sensitivity of DIAL or Raman scatter techniques for most gases.

11. SUGGESTED APPLICATIONS

Potential applications include determination of the following:

(1) Regional transport and dispersion, especially the effects of different source heights or locations. A portable lidar would be required.

(2) Dispersion in night-time stable conditions as a function of height.

(3) Transport and dispersion from different source locations in complex terrain.

(4) Flow and turbulence as drainage flows merge from connecting valleys.

(5) Trajectories in the lee of buildings or hills.

(6) Flow and turbulence near water/land and rural/urban interfaces.

(7) Dry deposition, by examining the dynamics of tracer movement above the surface in combination with concentrations of FPs collected on flat surfaces.

(8) Trajectories in gravity waves.

(9) Dispersion of puffs in the Lagrangian frame.

The most promising uses of multiple-FT lidar are those that take advantage of its remote-sensing character, excellent night-time sensitivity, and discrimination of several tracers. The two major drawbacks are poor performance with bright background light and limited SNR when only a small number of photons are received from ranges beyond a few kilometers from the lidar. A fixed site is adequate when measurements are needed only within these few kilometers of the lidar. A portable (airborne or truck-mounted) system is desirable to bring the lidar close to the tracers when transport over larger distances must be observed.

12. RECOMMENDATIONS FOR FUTURE RESEARCH

Testing of the multiple-FT lidar concept and evaluation of optimum configurations is recommended as a prelude to implementation for particular applications. These tasks should be completed:

(1) Demonstrate proper discrimination between tracers, with and without substantial levels of crosstalk.

(2) Evaluate a spectrometer for optical filtering in comparison with beam splitters followed by interference filters. Rejection of strong on-line scatter while maintaining high throughput of fluorescence is a key design factor.

(3) Measure FT signals in the 180° lidar mode to confirm the SNR and sensitivity analytically predicted from laboratory measurements of FT fluorescence.

(4) Develop efficient data-processing methods for simultaneous solution for concentrations (Eq. 14). (If the gain matrix **G** is constant from pulse to pulse, the transpose and inverse calculations must be made only once. However, if laser pulse energies or attenuation change, or optical and electronic factors are adjusted to follow changes in tracer concentrations, these matrix calculations must be repeated.)

(5) Develop and validate calibration procedures.

(6) Design and test aerosol generators to dispense tracers at adequate rates without undue clumping.

(7) Conduct further search, development, and testing of FTs for better performance and cost-effectiveness.

The quickest and least expensive way to accomplish these tests is probably through modification of an existing lidar system. A surface-based rather than airborne lidar is preferred for ease in testing with different equipment configurations and operational scenarios.

The field experiments should be performed at a site instrumented for wind measurements so the plume flux calibration method can be used. Elevation of tracer release and wind measurements to a substantial distance above the surface are desirable to minimize deposition loss, to allow the lidar to scan the entire plume cross section, and to have uniform wind speed through the vertical extent of the plume.

13. SUMMARY

Remote detection by lidar of the concentration of multiple fluorescent tracers of air motions would be an extension of a technique already demonstrated with a single FT (Rowland and Konrad, 1979b; Kyle et al., 1982; Uthe et al., 1985; and Karl, 1989). The fluorescence from FTs with different emission spectra could be spectrally filtered in the lidar receiver and simultaneously detected in optical channels with passbands near the peak of each emission. An analytical study based on laboratory measuarements showed that the multiple-FT lidar is feasible. This new atmospheric tracer technique would provide capabilities beyond those now available.

Two, or perhaps a few, widely separated laser wavelengths can excite an equal number of FTs with only a minuscule amount of crosstalk in their emission spectra to interfere with discrimination. With negligible crosstalk, the tracers would be independent, and each one could be treated individually during data analysis.

Two or more tracers can also be excited by closer, or even the same, laser wavelengths. However, overlapping emission spectra will almost surely introduce crosstalk into the optical passbands of the receiver. Matrix methods must then be used to solve the measurements for the concentration of each tracer when the number of detection channels equals or exceeds the number of tracers.

Lasers, detectors, and FPs are already commercially available for a multi-FT lidar system. Pigment particles that are commercially manufactured for fluorescent paints and inks have been used in a single-FT lidar system and should also perform well in a multiple-FT lidar. Common, harmless bacterial cells also have potential. Additional research is recommended to identify and optimize the FTs.

The equations in Sec. 7 can be used to calculate the number of photoelectrons per range gate from the FTs and the signal from all important interfering sources: crosstalk;

molecular Raman scatter; fluorescence from ambient aerosol particles and gases; background light; dark current; and leakage through the optical filter of on-line scatter from the atmosphere. The expressions given here for signal-to-interference ratio (SIR) and signal-to-noise ratio (SNR) are the first to include the effects of Raman scatter and shot noise.

The analysis shows that poor SNR associated with shot noise from weak fluorescent signal can sometimes limit measurement accuracy, even when the SIR is good. On the positive side, the interfering signals can usually be determined to good accuracy and subtracted from the FT signals. When this is successful and SNR is good, the concentration measurements can be satisfactory, even when SIR falls to 0.1 or below.

Matrix methods for determining the effect of measurement errors on the inferred concentrations are used to examine design tradeoffs and errors in a system with two tracers excited at one wavelength. An example with considerable overlap of the emission spectra illustrates a worst-case degree of crosstalk.

All else being equal, the performance of two tracers with crosstalk approaches that of two independent tracers, except for one major difference. When one tracer has much higher concentration than the other, the crosstalk can lead to significant errors in the fractional concentration of the more dilute tracer. The shot noise from the dense tracer masks the dilute tracer and thus raises the detection threshold of the latter. Relative calibration errors, i.e., incorrect ratios of the matrix elements in **G** (Eq. 14), can also cause large errors in the concentration of the more dilute tracer. If substantial crosstalk cannot be avoided, system design and experimental procedures should mitigate this error as much as possible. Interpretation of data must also account for any masking effects.

The shot noise, any crosstalk that must be endured, and the difficulty of optical calibrations prevent highly accurate concentration measurements except in ideal circumstances. We expect that, when needed, calibration procedures can yield concentration accuracies better than typical uncertainties (30–50%) in dispersion experiments caused by atmospheric variability and errors in other experimental data. Three calibration procedures are recommended whenever possible in conjunction with application of the technique:

(1) Use Raman scatter from N_2 or O_2 for field calibration of the sensitivity of the lidar. For instance, interchanging filters can remove almost all relative error between spectrally adjacent receiver channels.

(2) Make repeated scans of the cross section of a plume while monitoring the tracer release rate and the wind speed advecting the plume. These data allow calibration of the entire lidar-tracer system (Eberhard et al., 1987), including fluorescence efficiency of the tracer and optical characteristics of the lidar.

(3) Under field conditions, measure the signal from each tracer when all other tracers are known to be absent. The data from all channels affected by crosstalk can be used to fine-tune the relative calibration.

Potential applications can take advantage of three special characteristics of the multiple FT lidar technique: (1) the remote detection of tracer distributions in two or three spatial dimensions and time; (2) the sensitivity to low concentrations of FTs; (3) the ability for simultaneous measurement and discrimination between tracers. The main advantage of multiple-FT lidar rests with its comprehensive spatial or temporal coverage of the behavior of several tracers. A lidar can define the position and shape of the tracer plumes or clouds to a high degree of accuracy (Uthe et al., 1985b). This broad view of the tracers, along with extensive spatial averaging, can also help define instances one tracer might mask another. Although sequential releases of one tracer can provide information similar to simultaneous release of several tracers, the results are usually difficult to interpret because the meteorological conditions constantly change.

Multiple FTs could show the source-receptor relationships in regional transport. The dependence of dispersion on release location or conditions could be readily observed. Several tracers could reveal the structure of complicated flows, for example, in complex terrain, in the lee of hills or buildings, and near water-land interfaces.

Experimental demonstration of the multiple-FT lidar technique is recommended.

14. ACKNOWLEDGMENTS

The encouragement of J.L. McElroy is appreciated. E.R. Westwater guided us to the appropriate matrix methods. M. Goldberg measured the two-dimensional matrix of excitation and emission for the pigment FTs. This research was funded by the U.S. Environmental Protection Agency (EPA) through Interagency Agreement DW13932524-01-0 with the National Oceanic and Atmospheric Administration.

15. REFERENCES

Benson, R.C., and H.A. Kues, 1977: Absorption and fluorescence properties of cyanine dyes. *J. Chem. Eng. Data*, *22*, 379–383.

Berlman, I.B., 1965: *Handbook of Fluorescence Spectra of Aromatic Molecules*, Academic Press, 258 pp.

Ching, J.K.S., E.E. Uthe, B.M. Morley, and W. Viezee, 1984: Observational study of transport in the free atmosphere. *Proc., Fourth Joint Conf. on Applications of Air Pollution Meteorology*, Oct. 16–19, 1984, Portland, OR, American Meteorological Society, Boston, MA, 154–157.

Collis, R.T.H., and P.B. Russell, 1976: Lidar measurement of particles and gases by elastic backscattering and differential absorption. *Topics in Applied Physics, Vol. 14, Laser Monitoring of the Atmosphere*, E.D. Hinkley, Ed., Springer-Verlag, 71–151.

Deutsch, R., 1965: *Estimation Theory*, Prentice-Hall, 269 pp.

Eberhard, W.L., and Z.-Z. Chen, 1989: Lidar discrimination of multiple fluorescent tracers of atmospheric motions. *Appl. Opt.*, *28*, (in press).

Eberhard, W.L., and G.T. McNice, 1986: Versatile lidar for atmospheric studies, including plume dispersion, clouds, and stratospheric aerosol. *J. Atmos. Oceanic Technol.*, *3*, 614–622.

Eberhard, W.L., G.T. McNice, and S.W. Troxel, 1987: Lidar sensing of plume dispersion: Analysis methods and product quality for light-scattering tracer particles. *J. Atmos. Oceanic Technol.*, *4*, 674–689.

Gelbwachs, J., and M. Birnbaum, 1973: Fluorescence of atmospheric aerosols and lidar implications. *Appl. Opt.*, *12*, 2442–2447.

Inaba, H., 1976: Detection of atoms and molecules by Raman scattering and resonance fluorescence. *Laser Monitoring of the Atmosphere*, *Topics in Applied Physics*, *14*, E.D. Hinkley, Ed., Springer-Verlag, 153–236.

Jacobs, S.F., 1978: Nonimaging detectors. Section 4 of *Handbook of Optics*, McGraw-Hill.

Johnson, W.B., 1983: Meteorological tracer techniques for parameterizing atmospheric dispersion. *J. Climate Appl. Meteor.*, *22*, 931–946.

Karl, R.R. Jr., 1988: Experimental results of lidar observation of atmospherically dispersed vegetative cells and spores of live bacteria. *Abstracts, Fourteenth International Laser Radar Conference*, June 20–24, 1988, San Candido, Italy, International Radiation Commission, 81–84.

Karl, R.R. Jr., 1989: Field test results of atmospherically dispersed vegetative cells for a tracer using a solar blind fluorescence lidar. *Preprints, 6th Joint Conference on Applications of Air Pollution Meteorology*, January 30–February 3, 1989, Anaheim, American Meteorological Society, Boston, MA, 125–127.

Kerker, M., and S.D. Druger, 1979: Raman and fluorescent scattering by molecules embedded in spheres with radii up to several multiples of the wavelength. *Appl. Opt.*, *18*, 1172–1179.

Kyle, T.G., S. Barr, and W.E. Clements, 1982: Fluorescent particle lidar. *Appl. Opt.*, *21*, 14–15.

Lakowicz, J.R., 1983: *Principles of Fluorescence Spectroscopy*. Plenum Press, 496 pp.

Leighton, P.A., W.A. Perkins, S.W. Grinnell, and F.X. Webster, 1965: The fluorescent particle atmospheric tracer. *J. Appl. Meteor.*, *4*, 334–348.

Maeda, M., 1984: *Laser Dyes*. Academic Press, 335 pp.

Melfi, S.H., and D. Whiteman, 1985: Observation of lower-atmospheric moisture structure and its evolution using a Raman lidar. *Bull. Amer. Meteorol. Soc.*, *66*, 1288–1292.

RCA, 1974: *RCA Electro-optics Handbook*, RCA, Harrison, New Jersey, 255 pp.

Renaut, D., and R. Capitini, 1988: Boundary-layer water vapor probing with a solar-blind Raman lidar: Validations, meteorological observations and prospects. *J. Atmos. Oceanic Technol.*, *5*, 585–601.

Rowland, J.R., and T.G. Konrad, 1979a: A new technique for the study of power plant plume behavior using fluorescent dye as tracers and lidar as the remote sensor. Report S1R 79U-003, Appl. Physics Lab., Johns Hopkins Univ., Laurel, MD.

Rowland, J.R., and T.G. Konrad, 1979b: A new lidar-fluorescent tracer technique for atmospheric research and pollution studies. Report #S1R 79U–036, Appl. Physics Lab., Johns Hopkins Univ., Laurel, MD, 55 pp.

Schuster, B.G., and T.G. Kyle, 1980: Pollution plume transport and diffusion studies using fluorescence lidar. *Appl. Opt.*, *19*, 2524–2528.

Uthe, E.E., W. Viezee, and B.M. Morley, 1984: Airborne lidar monitoring of fluorescent dye particles as a tracer to characterize transport and dispersion: a feasibility study. Final Report, SRI Project 5782, SRI International, Menlo Park, CA, 120 pp.

Uthe, E.E., W.V. Viezee, and J.K.S. Ching, 1985a: Airborne lidar tracking of fluorescent tracers for atmospheric transport and diffusion studies. *Tech. Digest, Topical Meeting on Optical Remote Sensing of the Atmos.*, January 15–18, 1985, Incline Village, NV, Optical Society of America, Paper WC26.

Uthe, E.E., W. Viezee, B.M. Morley, and J.K.S. Ching, 1985b: Airborne lidar tracking of fluorescent tracers for atmospheric transport and diffusion studies. *Bull. Amer. Meteor. Soc.*, *66*, 1255–1262.

Voedisch, R.W., 1973: Luminescent pigments, organic. In *Pigment Handbook, Vol. I*, T.C. Patton, Ed., John Wiley and Sons, Inc., 891–903.

Weiner, E.R., and M.C. Goldberg, 1982: Optimizing the selectivity of standard spectrophotofluorometers with computer control. *American Laboratory*, 37–46.

Zuev, V.E., 1976: Laser-light transmission through the atmosphere. *Topics in Applied Physics, Vol. 14, Laser Monitoring of the Atmosphere*, E.D. Hinkley, Ed., Springer-Verlag, 29–69.

Appendix. Manufacturers of Fluorescent Pigment Particles

Some manufacturers of fluorescent pigment particles in the United States are listed. Additional vendors of such products may exist in this country or abroad.

Day-Glo Color Corporation
4515 St. Clair Avenue
Cleveland, Ohio 44103
(216) 391–7070

Lawter International, Inc.
990 Skokie Boulevard
Northbrook, Illinois 60062
(312) 498–4700

Radiant Color
2800 Radiant Avenue
Richmond, California 94804
(415) 233–9119